Supplement of Atmos. Chem. Phys., 25, 11789–11811, 2025
https://doi.org/10.5194/acp-25-11789-2025-supplement

Atmospheric Chemistry and Physics
Open Access

Supplement of

Complementary aerosol mass spectrometry elucidates sources of wintertime submicron particle pollution in Fairbanks, Alaska, during ALPACA 2022

Amna Ijaz et al.

Correspondence to: Amna Ijaz (amna.ijaz@pnnl.gov) and Barbara D'Anna (barbara.danna@univ-amu.fr)

The dataset comprising the ions detected and identified in this study is available with the DOI 10.5281/zenodo.14254283.

S1. Conversion from mixing ratios to mass concentrations

The mixing ratios in ppbV were calculated using **Equation S1**.

$$R = \frac{RH^+}{H_3O^+} \times \frac{Tr_{H3O^+}}{Tr_{RH^+}} \times \frac{U_{drift} \times T_{drift}^2}{k \times p_{drift}^2} \text{................} \textbf{Equation S1}$$

Where the RH^+ and H_3O^+ are the signal intensity in counts per second (cps) of the analyte and the reagent ions corrected according to their respective relative transmissions (Tr). U_{drift}, T_{drift}, and p_{drift} denote the voltage, temperature, and pressure (in mbar) in the drift tube, and *k* is the reaction rate coefficient (cm^3/s) between the reagent ion and a given volatilised analyte.
The Tr in the range of 21–135 amu was determined experimentally with a calibration gas mixture (12-component mix at ppmV level each from Apel Riemer Environmental Inc, Miami, USA) after 10-fold dilution with pure nitrogen at the beginning and at the end of the measurement campaign. The composition of the calibration gas mixture and the experimental sensitivity measured in the field are summarised in **Table S1**.

The value of *k* in **Equation S1** for the proton-transfer reaction between an analyte ion and $[H_3O]^+$ can be estimated theoretically. The Langevin−Gioumousis−Stevenson and the Su and Chesnavich theories are applied to pure hydrocarbons (Langevin, 1903) and oxygenated compounds (Su and Chesnavich, 1982), respectively. Both use the molecular weight (MW) and dipole moment (μ_D), while the former also includes polarizability (α) to predict ion-molecule reaction rates (Ellis and Mayhew, 2014). The values of *k* for organic compounds cover a wide range typically from $1.7–2.5\times10^{-9}$ cm^3/sec (Zhao and Zhang, 2004), while high values, up to 5.48×10^{-9} cm^3/sec (norpionaldehyde; $C_9H_{14}O_2$)(Cappellin et al., 2012) have been reported for oxygenated organic compounds. For quantification purposes, the standard protonation *k* of 2×10^{-9} cm^3/sec has been widely used (Holzinger et al., 2010; Capozzi et al., 2016; Pieber et al., 2018). This is expected to introduce a substantive error in quantifying most organic compounds, and thus, various estimation approaches have been proposed (Cappellin et al., 2012; Cappellin et al., 2010).

In this study, α was calculated using an elemental composition-based parameterisation for heteroatom-containing compounds following Sekimoto et al., (2017). For all other species with known elemental compositions, the parameterisation of Bosque and Sales (Bosque and Sales, 2002) was applied. For unknown species (no formula assigned), another parameterisation based solely on MW was used (Sekimoto et al., 2017). The range of α varied from 3.25×10^{-30} (for HNO_3) – 5.435×10^{-29} (for $C_{30}H_{48}O$). For heteroatom-containing species, μ_D were predicted based on elemental composition and/or MW (Sekimoto et al., 2017). For unknown species, a constant μ_D of 2.75 was used considering a predominance of oxygenated hydrocarbons (Müller et al., 2017). The final range thus obtained was 1.30–2.75 D. In a previous study, a constant μ_D of 2.75 and polarizabilities based on elemental composition were associated with quantification uncertainty of ±40% in the mass concentrations (Müller et al., 2017). MW and heteroatomic classes reduce uncertainties in the calculated *k* values (Sekimoto et al., 2017); thus, they were used to improve quantification accuracy. The *k* values calculated here for hydrocarbons were in close agreement with rates reported in the literature (**Figure S1**). In other cases, they were poorly aligned with previously reported protonation *k*-rates, due to the presence of different polarisable functional groups in species with the same empirical formula. For instance, proton-transfer *k* of 3.58×10^{-9}, 2.69×10^{-9}, 2.51×10^{-9}, and 3.32×10^{-9} cm^3/sec have been reported for acetone, oxetane, 2-propen-1-ol, and propanal (Cappellin et al., 2012), respectively, despite the same empirical formula (i.e., C_3H_6O). Such isomers cannot be differentiated in high-resolution mass spectrometry, and thus, only the general elemental composition is used to estimate the values of *k*. When the formula assignment is unambiguous, the relative uncertainty regarding the concentration derived from the propagation of the relative uncertainties on the transmission and the *k* is estimated to be within ±30% (Ellis and Mayhew, 2014). Due to the higher *k* values, the mixing ratios and mass concentrations measured here are expected to be underestimated. Specifically, mixing ratios and mass concentrations were 38.79 and 42.06% lower than those calculated with the standard value of $k = 2\times10^{-9}$ cm^3/sec.

Mass concentrations associated with individual ions were calculated by using the standard method (Seinfeld and Pandis, 2016) expressed in **Equation S2**.

$$\text{Mass concentration } (\mu g/m^3) = \left(\frac{P \times \left(\frac{m}{z}\right) - 1.0072765}{8.314 \times T}\right) \times mixing\ ratio\ (ppm) \ \ldots\ldots\ldots\ldots\ldots\ldots \textbf{Equation S2}$$

Where P, *m/z*, and T denote ambient pressure (in Pascals), the measured mass-to-charge of the ion, and ambient temperature (in Kelvin). 1.0072765 and 8.314 are the mass of a proton (in kg) and the molar gas constant (J/K/mol).

S2. Assignment of molecular formulae

Molecular formulae were assigned to accurate *m/z* measured with the PTR_{CHARON} (*m/z* 50–425) using the following constraints: $C_cH_hO_oN_{0\text{-}3}S_{0\text{-}1}$ (number of C, H, and O were unrestricted), $-13 \leq$ DBE-O ≤ 20 (integer DBE values only); $0 \leq$ O/C ≤ 2.0; and $0.1 \leq$ H/C ≤ 3. Species assigned ^{13}C were retained for quantification and factorisation. Elemental composition was obtained with an average formula error of **1.23 ± 23.54 ppm** (ranging between -63.26 and 146.52 ppm). Relatively broad *m/z* accuracy and a mass resolution (Δ*m/m*) of ~5000 inevitably returned multiple prospective formulae for every ion. Both the selected formula and the second likely candidate are presented in the supplementary information, where the former was chosen based on the following priorities: lower number of heteroatoms > lower formula error > relevance to atmospheric emission sources identified here. Among the 1118 ions resolved, 336 were retained above the S/N, and 318 could be chemically identified in this way. Associated parameters (e.g., concentration-weighted O/C, H/C, etc.) were derived for total OA as described previously (Müller et al., 2017).

The following equation was used to calculate the relative importance of a variable (i.e., *formula*) in a factor.

$$RI_{i,f} = \frac{C_{i,f}^{norm} - C_{i}^{norm}}{\sigma_{i}^{norm}} \ \ldots\ldots\ldots\ldots\ldots\ldots \textbf{Equation S3}$$

Where

$RI_{i,f}$ = the relative importance of variable *i* in factor *f*
$C_{i,f}^{norm}$ = normalised concentration of variable *i* in factor *f*
C_{i}^{norm} = mean normalised concentration of variable *i* across all factors
σ_{i}^{norm} = standard deviation of the normalised concentration of variable *i* across all factors

S3. Concentration-weighted average enrichment factor (EF)

The EF of particles sampled by the CHARON inlet is dependent on their size as demonstrated in **Figure S2**. Particles larger than 150 nm have been reported to undergo enrichment of ~25 (Eichler et al., 2015b) or ~44-fold (Müller et al., 2017) in the aerodynamic lens. The EF reduces steeply for particles of <60–150 nm (Eichler et al., 2015b). Here, the distribution of mass concentrations across particles of 15–661 nm was calculated from particle number and density measured with a scanning mobility particle sizer (SMPS). **Figure S3** indicates that particles of 100–250 nm are predominant during the ALPACA campaign. In the dataset obtained from PTR_{CHARON} measurements, it is not possible to connect individual ions detected at any specific sampling time with a unique particle size or range of sizes. Therefore, we calculated the concentration-weighted average EF for $k = 1{:}n$ measurements using **Equation S4**. The time series for EF thus obtained is shown in **Figure S3**. The detected concentrations were then converted to sampled concentrations by dividing them with the corresponding EF value.

$$EF_{weighted} = \frac{\sum_{k=1}^{k=n} EF_k \cdot Conc_k}{\sum Conc} \ldots\ldots\ldots\ldots\ldots\ldots \textbf{Equation S4}$$

S4. Commentary on levoglucosan fragmentation and total OA quantification

Where required for the sake of discussion, uncorrected and corrected total OA (using a previously described method (Leglise et al., 2019)) from PTR_{CHARON} are denoted as OA_{uncorr} and OA_{corr}, respectively. Although PTR is a soft ionisation mechanism, when it is applied to large and heavily functionalised molecules, such as levoglucosan, fragmentation is inevitable (Müller et al., 2017; Leglise et al., 2019). Fragment and precursor ions cannot be distinguished in mass spectra generated for ambient air due to the molecular complexity. However, in our study, owing to the strong influence of biomass burning as a significant source of emissions, *m/z* 163.06 was a dominant ion. It was attributed to $C_6H_{10}O_5$ (levoglucosan and anhydrous monosaccharide isomers). It could unambiguously be associated with its known fragments at *m/z* 85 ($C_4H_4O_2$), 127 ($C_6H_6O_3$), and 145 ($C_6H_8O_4$) due to high correlation coefficients between the precursor and fragments ($R^2 > 0.95$; **Figure S4**). It must be noted that the possibility of isomers on the *m/z* values associated with levoglucosan fragments cannot be entirely ruled out. Like a previously reported PTR_{CHARON} analysis of pure levoglucosan (Müller et al., 2017), these fragment ions were more intense than the molecular ion, $[M+H]^+$.

Strong fragmentation of oxygenated compounds, such as levoglucosan and *cis*-pinonic acid, in ambient aerosol leads to an underestimation of total mass concentrations by 32–33%. Here, correcting for the fragmentation of levoglucosan only (i.e., by adding the mixing ratios calculated for the fragments to those of the precursor ion before conversion to mass concentrations with **Equation S2**) improved OA_{uncorr} by 5%; the total OA concentrations thus obtained are referred to as OA_{corr_levo}. A greater increase of 17% was observed in OA_{uncorr} upon fragmentation correction with the method of Leglise et al. (Leglise et al., 2019) as compared to correction for levoglucosan fragmentation only. This indicated that levoglucosan was not the only molecule prone to fragmentation based on molecular composition, and a more holistic approach to fragmentation correction is preferable. Therefore, the results presented herein report OA_{corr}, rather than OA_{corr_levo}. However, where required for the quantification of levoglucosan alone (such as the results in **Figure S9A**), OA_{corr_levo} was used.

In the case of the AMS, calibrations conducted during the ALPACA campaign with pure levoglucosan indicated *m/z* 60, i.e., $C_2H_4O_2$, to constitute 12% of the overall signal for levoglucosan. This quantitative relationship was used to estimate levoglucosan in ambient OA and is expected to provide an upper bound for the estimation, considering that other compounds can also contribute to the signal at *m/z* 60.

S5. Specifics of the factorisation of PTR_{CHARON} measurements

A preliminary unconstrained factorisation of the PTR_{CHARON} (mixing ratios used at this stage of analysis) did not delineate on-road traffic as a source unless the number of factors was allowed to be unreasonably high (e.g., >19 factors). However, a factor identified as ‘ road transport gasoline’ constituted a significant fraction of total VOCs in gas-phase PTR-ToF MS measurements during the ALPACA campaign (Temime Roussel et al., 2022). We used the time series of this gas-phase mobile gasoline factor to constrain the PMF of PTR_{CHARON} measurements, which helped isolate a reasonable on-road transport factor, albeit with very low concentrations of OA in it.

A cooking (COA) factor was observed in the unconstrained PMF trial, but it suffered from mixing with the transport and oxygenated OA (OOA) factors. To optimise it, we used the time series of a clean-looking COA factor from an unconstrained solution as an anchor and configured subsequent PMF runs to isolate this factor first. Once an eight-factor solution was established as the base-case (**Table S2**), 125 bootstrapping replicates were run, where COA and on-road transport factors were constrained with random *a*-values between 0 and 0.3 with a step-size of 0.05. This range of *a*-values was chosen to allow reasonable divergence of the factor from the anchor (i.e., up to 30%) while maintaining a strong correlation (at least 70%) with it.

We chose to leave the remaining factors unconstrained to take full advantage of the factor speciation possible with the molecular-level data from PTR_{CHARON}. The criteria used to select reasonable bootstrapped runs are listed in **Table S3**. Seventy-four runs (52.9%) passed the evaluation criteria for further analysis and were satisfactorily classified as distinct and unmixed (Stefenelli et al., 2019). The source apportionment results presented throughout the text (for AMS datasets as well) are an average of these selected runs. The mixing ratios apportioned to each factor were converted to mass concentrations and corrected for fragmentation with excellent agreement between the measured and factorised OA concentrations (**Figure S5**).

The factorisation of PTR_{CHARON} produced a unique factor that comprised mainly of very small ions of *m/z* < 65, labelled as the small molecules (SM) factor. This factor could not be assigned an environmentally relevant identity due to a lack of correlations with external tracers, and therefore, it has not been discussed in the main text. Its principal constituents were small species, such as *m/z* 59.05 (C_3H_6O), 61.03 ($C_2H_4O_2$), 73.03 ($C_3H_4O_2$), 75.04 ($C_3H_6O_2$), etc., that are expected to be in the gaseous phase, rather than the condensed phase. Its average concentration was **0.2 ± 0.1 µg/m^3** with significant relative contributions to total OA (>80%) during short and clean periods of the campaign, when ambient OA_{CHARON} was below 1 µg/m^3. We speculate that the SM factor is an artefact produced by instrumental chemical background and possible remnants of VOC species on the denuder as we switched from collecting gas-phase samples to particle sampling through the CHARON inlet.

S6. Specifics of the factorisation of AMS measurements

In both (organics only and organics + inorganics) the AMS analyses, O^+ (*m/z* 16), OH^+ (*m/z* 17), H_2O^+ (*m/z* 18), and CO^+ (*m/z* 43) were calculated as constant fractions of CO_2^+ (*m/z* 44), rather than being measured. They were thus excluded from PMF to avoid giving extra weight to CO_2^+ and reinserted into the profiles after factorisation (Xu et al., 2016; Datalystica, 2022). Unconstrained factorisation of AMS (measurements not corrected for CDCE or RIE at this stage) did not delineate an optimal unmixed COA factor in either AMS_{org} or $AMS_{org+inorg}$ datasets until six or more factors were allowed; this caused splitting and mixing of the hydrocarbon-like (HOA) or the biomass-burning OA (BBOA) factors. Primary factors, other than BBOA, were thus constrained using profiles obtained from suitable unconstrained runs. BBOA was left unconstrained with the same intention as in PTR_{CHARON}, i.e., to leave room for the separation of multiple biomass-based fuels. Four and six-factor solutions were chosen as the most reasonable choices for AMS_{org} and $AMS_{org+inorg}$, where only HOA and COA factors were constrained (**Tables S3**).

250 bootstrapping replicates each were run for the two datasets with random *a*-values between 0 and 0.3 with a step-size of 0.05. The evaluation criteria for selecting reasonable runs are listed in **Table S3**, which led to the selection of 200 (80%) and 249 (99.6%) distinct and unmixed runs (Stefenelli et al., 2019), respectively. After PMF analysis, matrices of factors from AMS_{org} and $AMS_{org+inorg}$ measurements were corrected for CDCE and RIE as described in a previous study (Zografou et al., 2022) using the CDCE and RIE values stated in **Section 2.2.2**.

Section S7. Positive matrix factorisation of size distributions from SMPS

PMF inputs require an error matrix, which was prepared using the method of Rivas et al., (2020) for both number and mass concentrations; only the results from the mass concentration analysis are discussed in this study. Briefly, the final uncertainty at each sampling point was measured as **α × (measured concentration + average concentration of a given size bin) + (C_3 × measured concentrations)**. Recommended α and C_3 range from 0.005–0.04 and 0.05–0.15 and were found to be optimum at 0.0175 and 0.1 for our matrix of mass concentrations. The optimisation was achieved based on the least scaled residuals. To remove noisy data, size bins with average concentrations lower than 10% of the entire matrix's average were removed leaving behind 96 size bins from 21.7 to 661 nm.

To find sizes corresponding to the PTR_{CHARON} or $AMS_{org+inorg}$ factors, fully constrained PMF trials with eight and six factors were run on SoFi with 10 calls in each. The time series of the factors of interest were used as anchors with an exact *a*-value of 0.1 (i.e., 10% divergence). Results of all calls were averaged. Bootstrapping was redundant due to the fully constrained nature and tight *a*-values used in these PMF trails.

S8. Discrepancies in mass concentrations of HOA/on-road transport emissions from PTR$_{\text{CHARON}}$ and AMS analysis

A significant quantitative discrepancy is observed between the OA contributions measured for on-road transport-related factors using PTR$_{\text{CHARON}}$ and AMS$_{\text{org}}$. On average, **2.1 ± 3.0 µg/m^3** of OA was associated with HOA$_{\text{AMS,org}}$, compared to only **0.1 ± 0.1 µg/m^3** for the transport$_{\text{CHARON}}$ factor (**Figure 6**). The slope of the scatter comparing HOA$_{\text{AMS,org}}$ and road transport$_{\text{CHARON}}$ suggests that the OA mass apportioned to the latter was only ~2% of that apportioned to the former (Table S4). This discrepancy could have several reasons. First, instrumental biases, i.e., the tendency of alkanes from gasoline to undergo dissociative PTR ionisation (Gueneron et al., 2015) and the limited ability of PTR$_{\text{CHARON}}$ to analyse particles smaller than 150 nm (Eichler et al., 2015a; Eichler et al., 2015b) are essential considerations. Indeed, the laboratory quantification of standard compounds by the PTR$_{\text{CHARON}}$, including alkanes (hexadecane, octadecane, eicosane, docosane, hexacosane, etc.), fatty acids (palmitic, oleic, stearic acid, etc.), and biomass burning markers (levoglucosan, vanillic, acid, coniferaldehyde, acetosyringone, etc.) revealed that alkanes are underestimated by 2–4 times their actual concentrations while the O-containing species remained unaffected. Furthermore, a fully constrained PMF of SMPS matrices (see **Section S7**) is shown in **Figure S12**, where peaks in road transport$_{\text{CHARON}}$ concentrations coincide with peaks in the contribution of particles sized 50–100 nm.

Lastly, an analysis of the relative variation in HOA$_{\text{AMS,org}}$ and NO$_x$ based on a previous approach (Zhang et al., 2019) provided evidence that non-vehicular emissions (specifically, heating oil combustion) also contribute to HOA$_{\text{AMS,org}}$, rendering its concentrations different from those of road transport$_{\text{CHARON}}$. The HOA/NO$_x$ ratio in the ALPACA campaign was up to 5× higher during the evening than during the morning (data not shown); considering that NO$_x$ is majorly emitted from vehicles in Fairbanks, this ratio should remain consistent through the day if HOA were also released from vehicles only. The diurnal patterns provide insight into an additional source: while tracers of vehicular emissions, NO$_x$ and BC, decreased continuously from 18:00 hrs onwards, HOA$_{\text{AMS,org}}$ and the HOA/NO$_x$ ratio decreased from 18:00 hrs and then increased again from 20:00 hrs onwards, which coincides with residential heating emissions. Collectively, these aspects provide plausible reasons for the critical quantitative differences in the transport$_{\text{CHARON}}$ and HOA$_{\text{AMS,org}}$ factor.

S9. Discrepancies in mass concentrations of the cooking factor from PTR$_{\text{CHARON}}$ and AMS analysis

Similar to HOA$_{\text{AMS,org}}$ and transport$_{\text{CHARON}}$, the OA mass concentrations apportioned to COA exhibited some difference between the two instruments (COA$_{\text{AMS,org}}$ = **0.6 ± 0.8 µg/m^3**; COA$_{\text{CHARON}}$ = **0.1 ± 0.2 µg/m^3**; **Figure 6**) with a temporal correlation (R^2) of 0.47 (**Table S4**). Like HOA, these differences are partly attributable to the particle size, as a greater contribution of cooking emissions to OA is observed for particles centred around ~100 nm (**Figure S12A**). Another potential explanation could be related to an overestimation of COA with the AMS, as standard RIE of 1.4 was used for organics; recent studies have reported an overestimation of COA by the AMS compared to co-located instruments, such as the chemical ionisation mass spectrometer and SMPS, and suggested a RIE varying from 1.5 up to 3.1 (Reyes-Villegas et al., 2018) and 4.3–6.5 (Katz et al., 2021). However, these studies focused on fresh indoor or laboratory-generated cooking emissions. For instance, in our research, the COA factor presented low O/C ratios of 0.17, 0.11, and 0.09 with the PTR_{CHARON}, AMS_{org}, and $AMS_{org+inorg}$, respectively, indicating fresh emissions, which is due to the proximity of CTC, UAF to restaurants and urban areas.

Supplementary figures

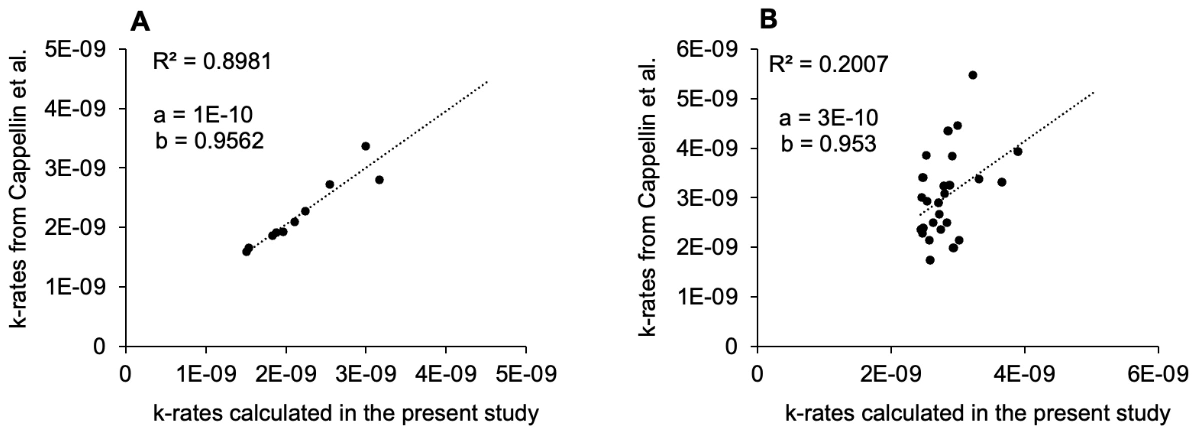

Figure S1. Assessing the agreement between protonation rate coefficients (*k*-rates) predicted in this study and those estimated by (Cappellin et al., 2012) for (**A**) hydrocarbons and (**B**) heteroatom-containing species.

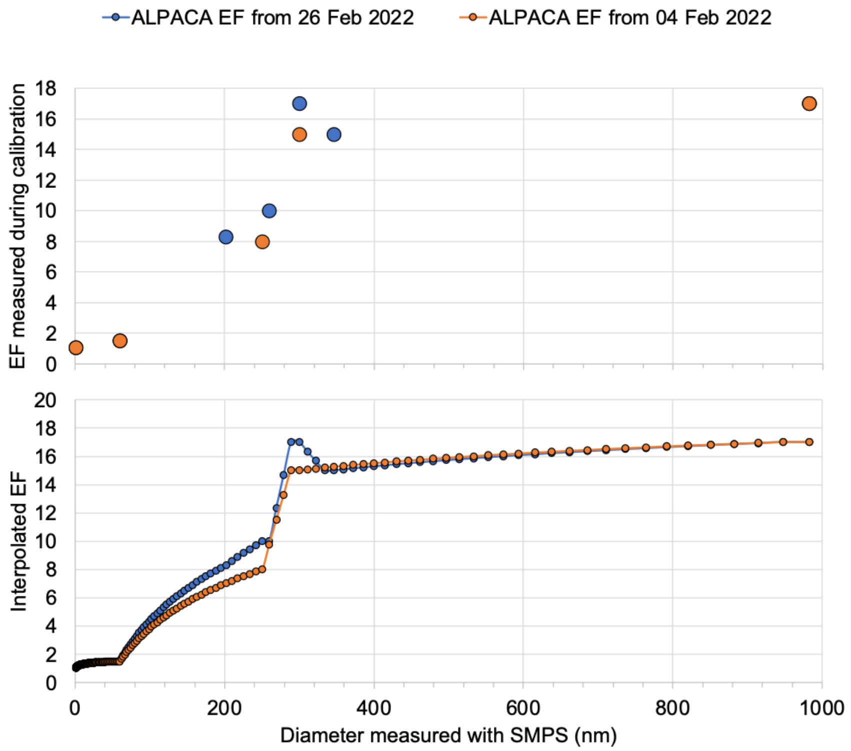

Figure S2. Overview of enrichment factors (EF) used in this study. (**A**) EF measured from calibrations with pure levoglucosan during the ALPACA campaign for particles of specific sizes; and (**B**) interpolation of EF across the complete range of particle sizes from 15–1000 nm.

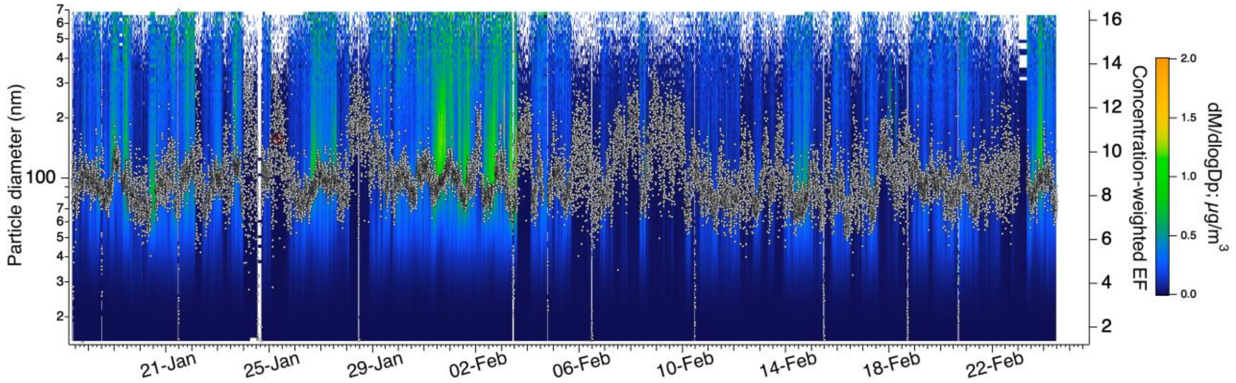

Figure S3. Particle size distribution from an SMPS. Gray data points represent the average enrichment factor (EF) weighted to these mass concentrations. This time series was generated using the calibration curve from Feb 26, 2022 (shown in Figure S2).

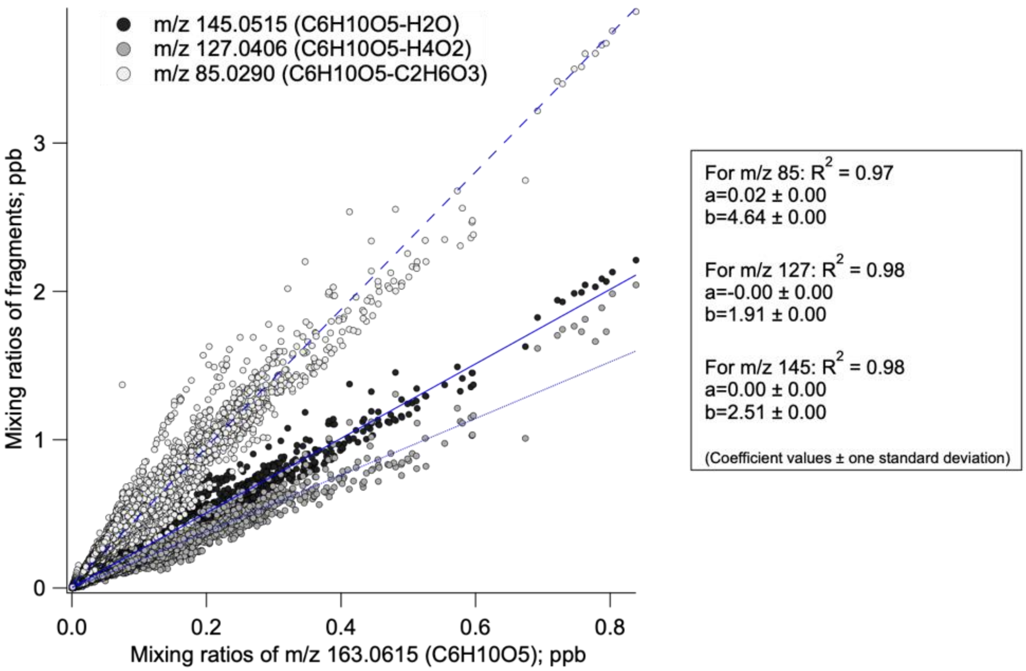

Figure S4. Scatter plot to show the correlation ($p \leq 0.05$) between the mixing ratios of levoglucosan (*m/z* 163) and its expected fragments at *m/z* 85, 127, and 145.

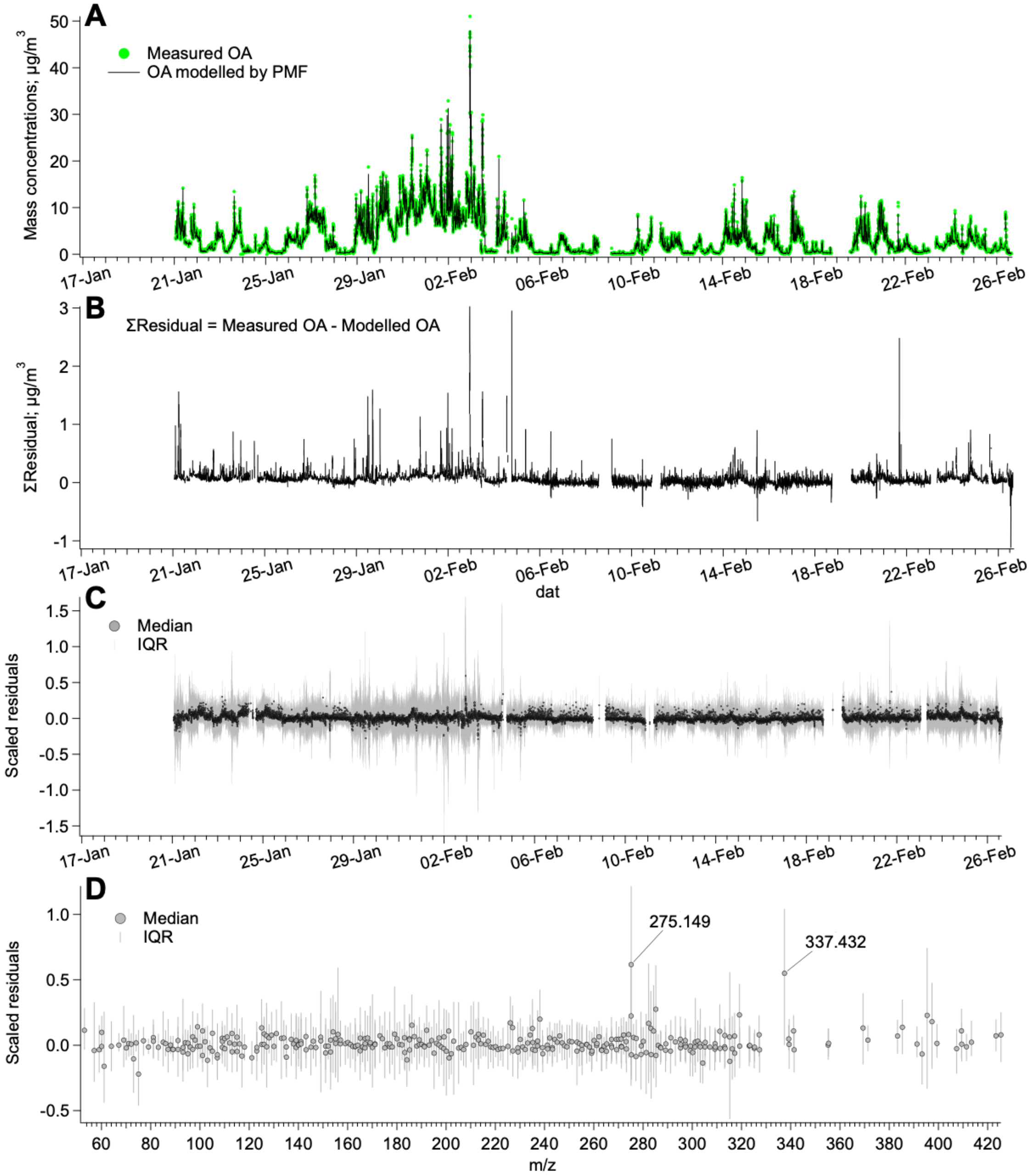

Figure S5. Diagnostics for the positive matrix factorisation of $\mathrm{PTR}_{\mathrm{CHARON}}$ measurements. (**A**) Total measured OA and the sum of OA apportioned to all eight factors, i.e., the so-called *modelled* OA; (**B**) Sum of residuals; (**C**) Scaled residuals in the time series; and (**D**) Scaled residuals in the mass spectra. The median and interquartile range (IQR) of the scaled residuals for 75 runs (total runs = 125) selected after bootstrapping are shown. *Note: Scaled residuals indicate how well the PMF model fits the measurements and how much of the variability in the input data remains unexplained (Juntto and Paatero, 1994); ideally, they should be within ± 2.*

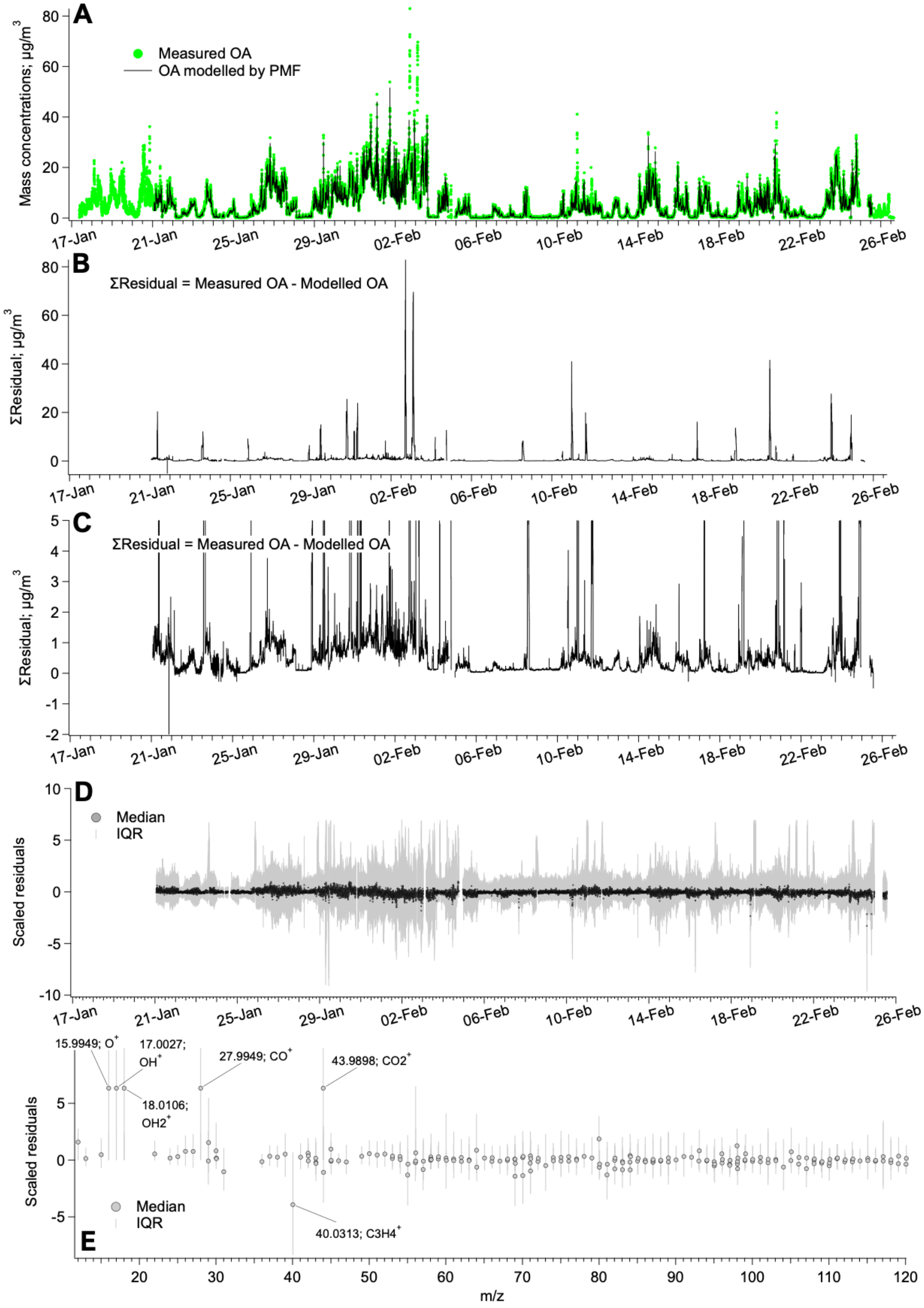

Figure S6. Diagnostics for the positive matrix factorisation of AMS_{org} measurements. (**A**) Total measured OA and the sum of OA apportioned to all four factors, i.e., the so-called *modelled* OA; (**B–C**) Sum of residuals, where C is zoomed-in at low concentrations; (**D**) Scaled residuals in the time series; and (**E**) Scaled residuals in the mass spectra. The median and interquartile range (IQR) of the scaled residuals for the 200 runs (total runs = 250) selected after bootstrapping are shown. *Note: Please see **Figure S5** for the definition of scaled residuals*

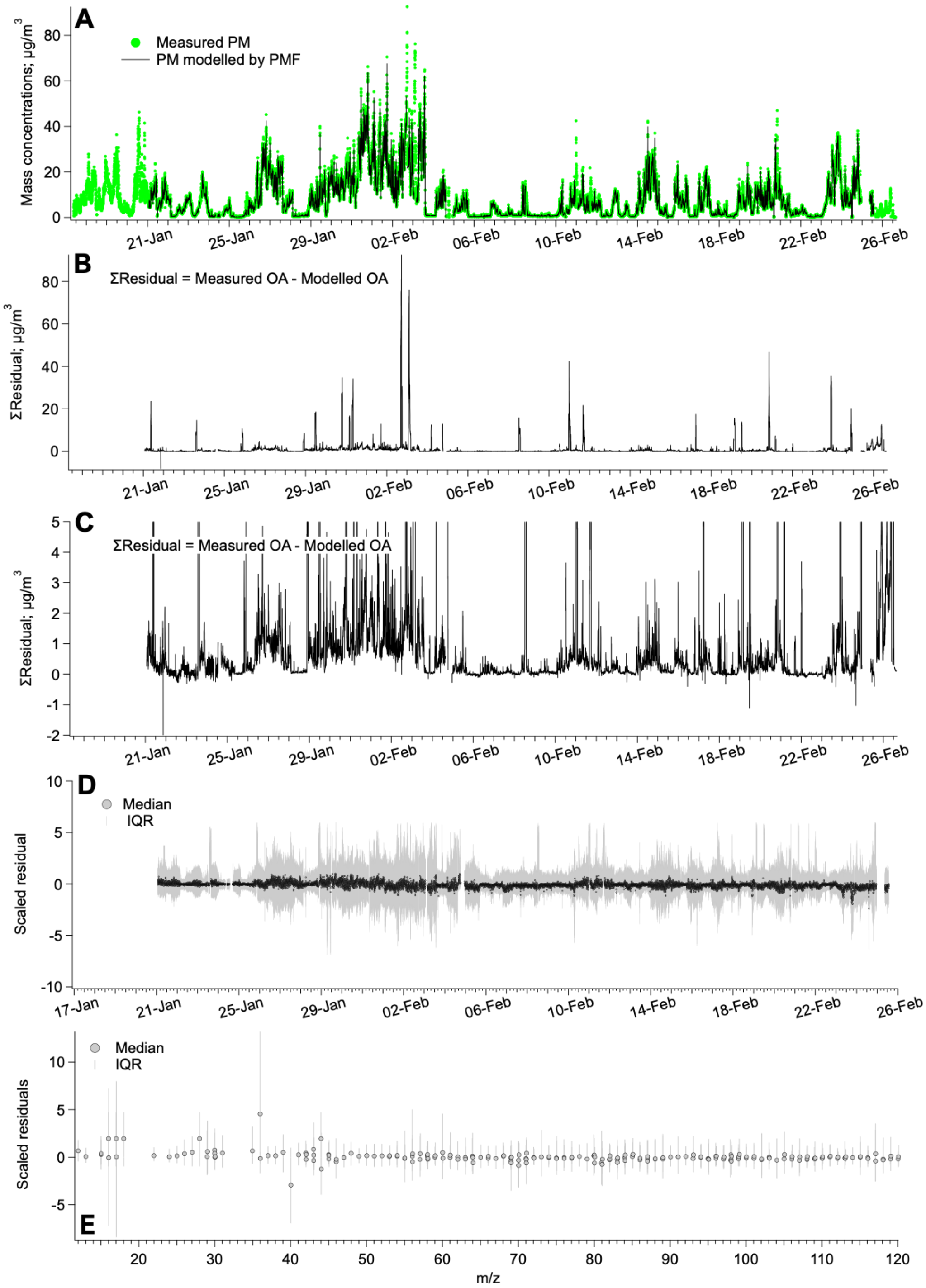

Figure S7. Diagnostics for the positive matrix factorisation of AMS$_{org+inorg}$ measurements. (**A**) Total measured NR-PM$_1$ and the sum of NR-PM$_1$ apportioned to all six factors, i.e., the so-called *modelled* NR-PM$_1$, (**B–C**) Sum of residuals, where (C) is zoomed-in at low concentrations, (D) Scaled residuals in the time series, and (E) Scaled residuals in the mass spectra. The median and interquartile range (IQR) of the scaled residuals for the 249 runs (total runs = 250) selected after bootstrapping are shown. *Note: Please see **Figure S5** for the definition of scaled residuals.*

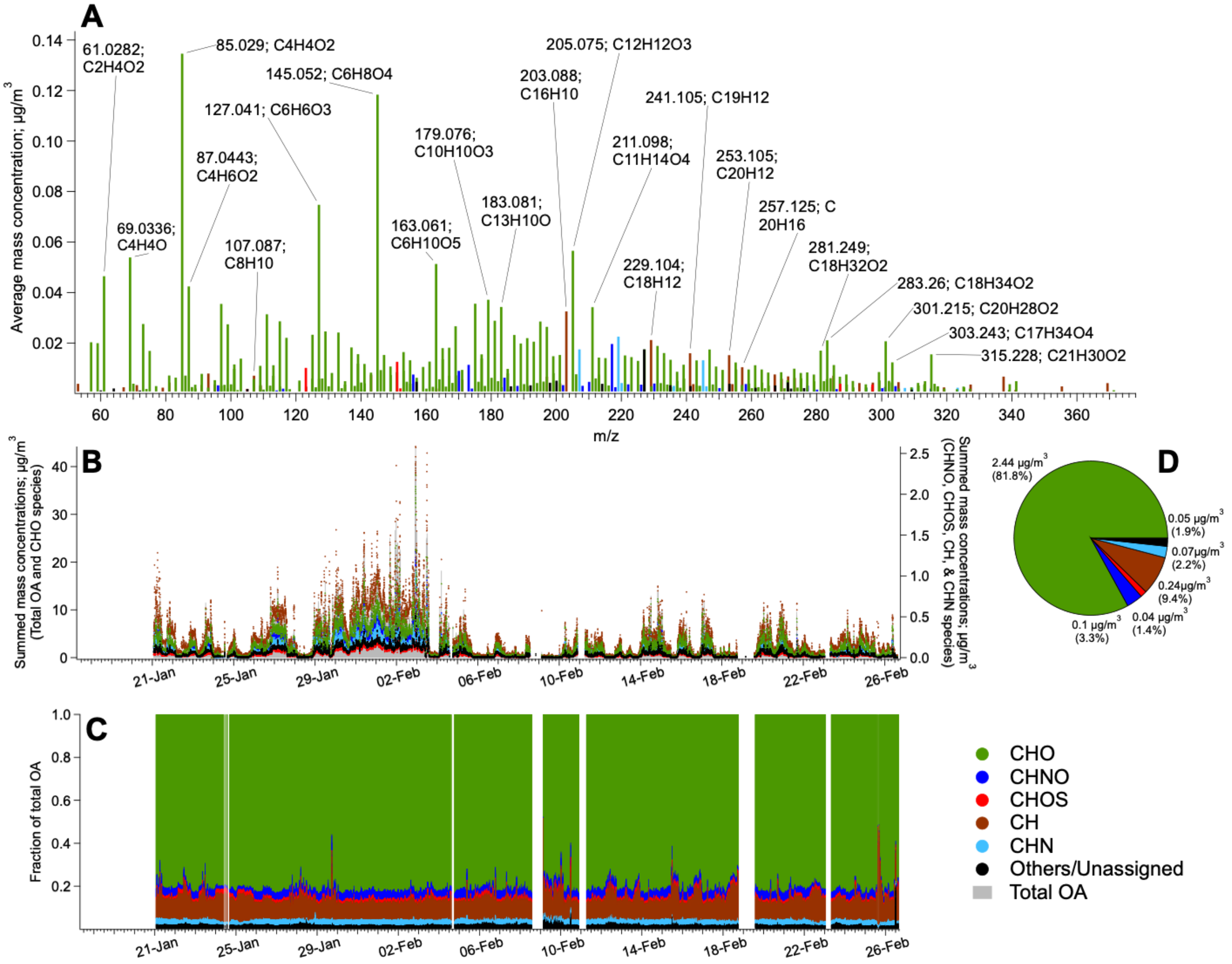

Figure S8. Molecular composition of ambient OA from PTR_{CHARON}. (**A**) Mass spectra of ion concentrations averaged over the campaign; (**B**) Time series of species belonging to the five molecular groups: CHO, CHNO, CHOS, CH, and CHN. Species that could not be assigned a formula are shown as the black; and (**C**) fractions of the aforementioned molecular groups in the total OA_{CHARON} mass.

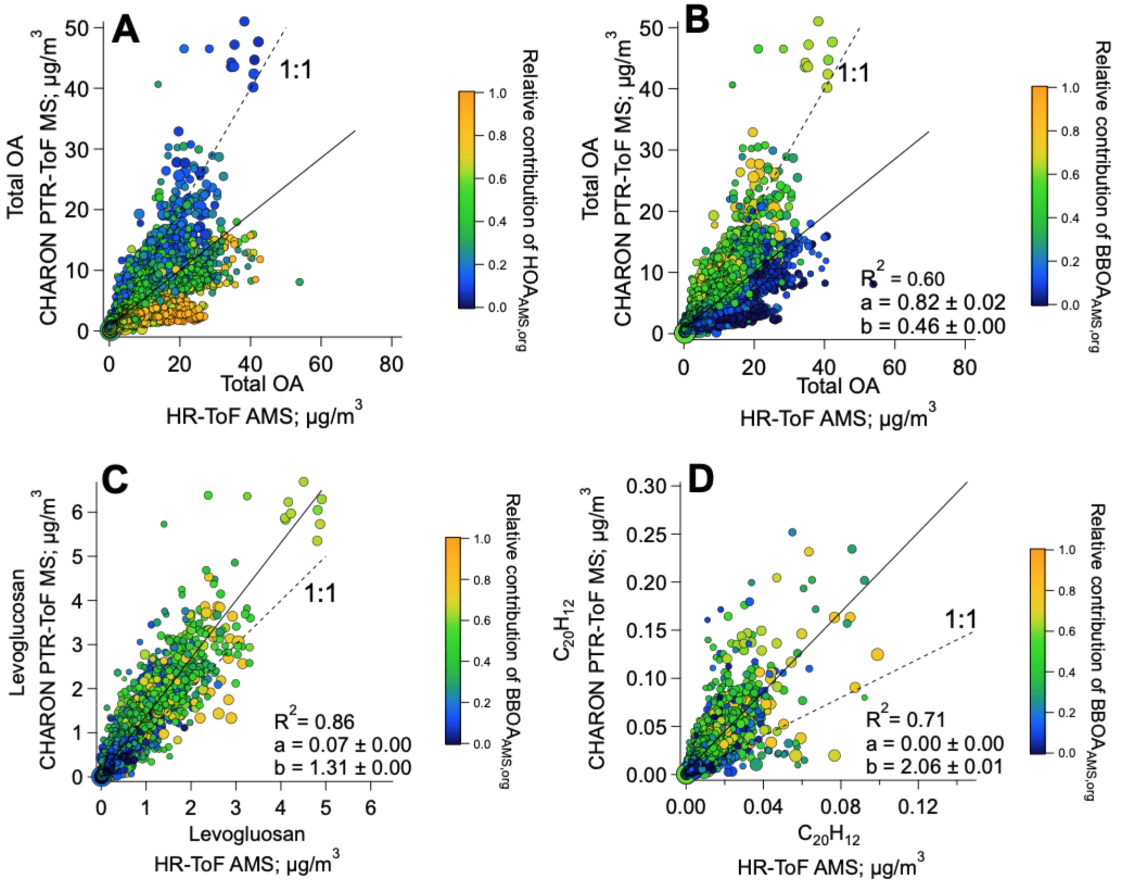

Figure S9. Scatter plots showing the linear regression ($p \leq 0.05$) of (**A–B**) total OA measured with the AMS and the $\text{PTR}_{\text{CHARON}}$ coloured by the relative contribution of biomass burning OA and hydrocarbon-like OA factors diagnosed in AMS analysis, (**C**) levoglucosan and (**D**) $C_{20}H_{12}$ (assumed to be a PAH that was estimated using the method of (Herring et al., 2015)) measured with the AMS and $\text{PTR}_{\text{CHARON}}$. In (**C**) and (**D**) data points are coloured by the relative contributions of the BBOA factor diagnosed in AMS measurements. Data points are sized by the geometric mean mass of the dM/dlogDp calculated from the SMPS (50 to 500 nm). The dashed line denotes the 1:1 relationship. Coefficients, *a* and *b*, represent the slope and the intercept for the linear regression ($p \leq 0.05$; solid line) and are written with ± one standard deviation.

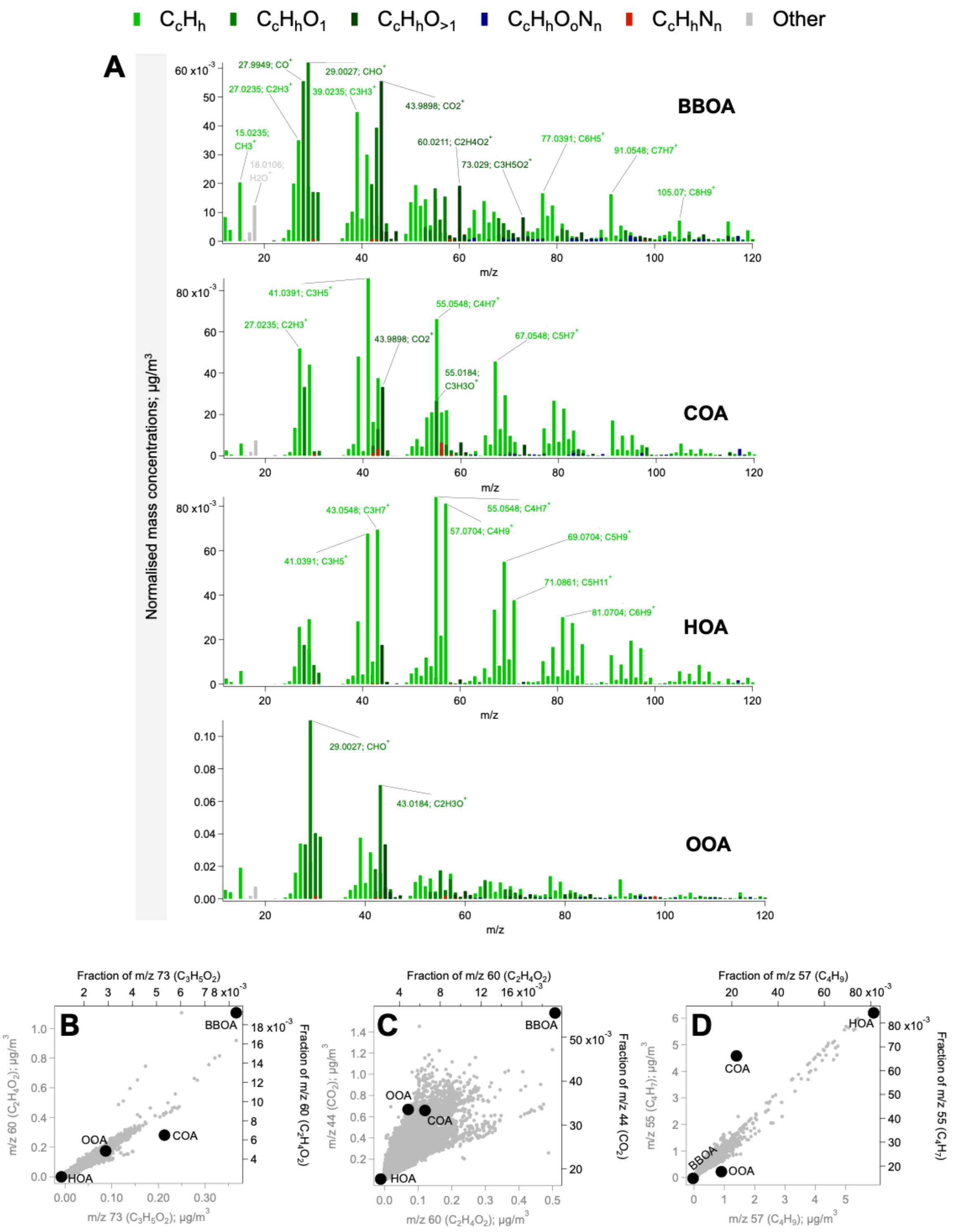

Figure S10. Overview of the factorisation output for AMS_{org} measurements. **(A)** Normalised mass spectra of factors coloured by the elemental composition of the fragments. Mass concentrations are normalised to the sum of the concentrations of all ions. Comparison of the absolute concentrations in ambient OA (grey data points; bottom and left axes) and fractional contribution in each factor (black data points; top and right axes) of (**B**) *m/z* 60 versus *m/z* 73; (**C**) *m/z* 44 versus *m/z* 60; and (**D**) *m/z* 55 versus *m/z* 57.

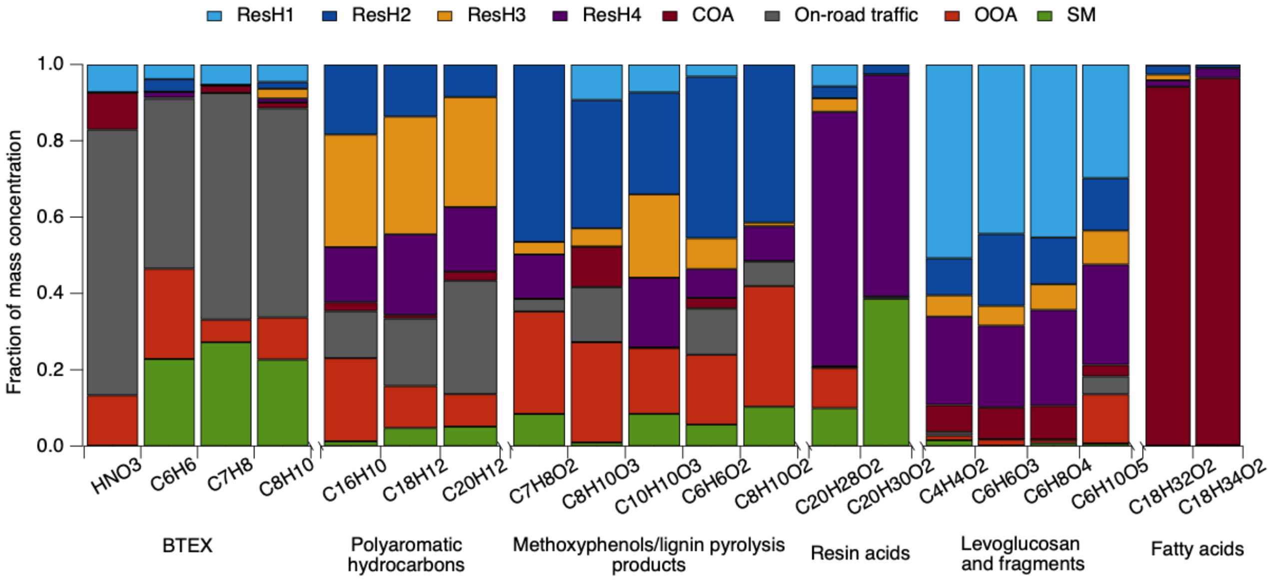

Figure S11. Fraction distribution of key markers species in the eight factors diagnosed for OA measured with the PTR$_{\text{CHARON}}$.

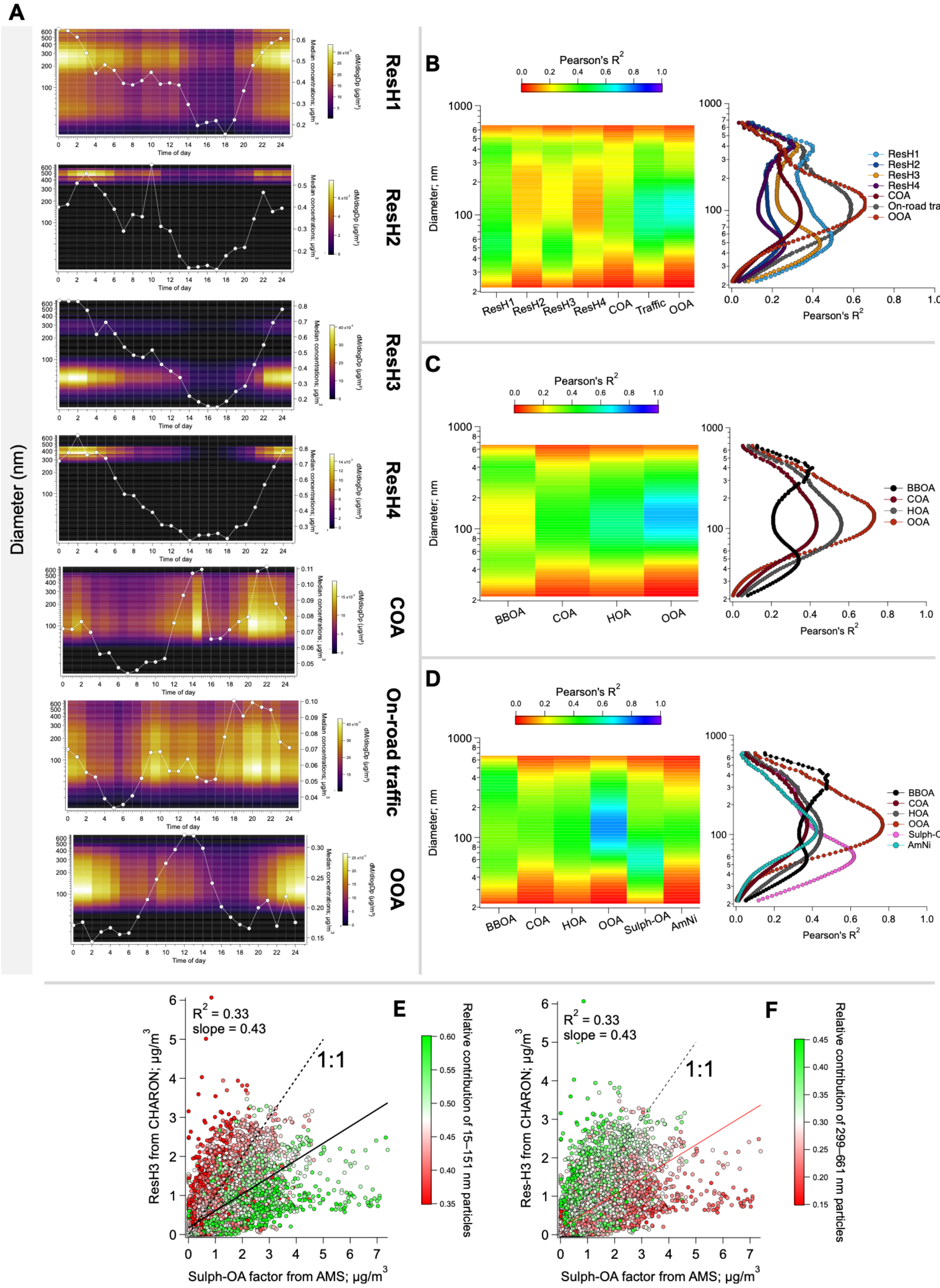

Figure S12. Particle mass size distributions from SMPS for all factors identified in this study. (**A**) Diurnal trends for PTR_{CHARON} factors and their corresponding particle sizes; (**B-D**) Linear regression ($p < 0.05$) over time between the particle size bins and factors in PTR_{CHARON}, AMS_{org}, and $AMS_{org+inorg}$ analysis, respectively. Please see **Section S7** for the methodology of SMPS analysis; (**E-F**) scatter plot of sulph-OA and ResH3 factor from PTR_{CHARON} analysis coloured by the relative contributions of smaller (15–151 nm) and larger (299–661 nm) aerosol particles.

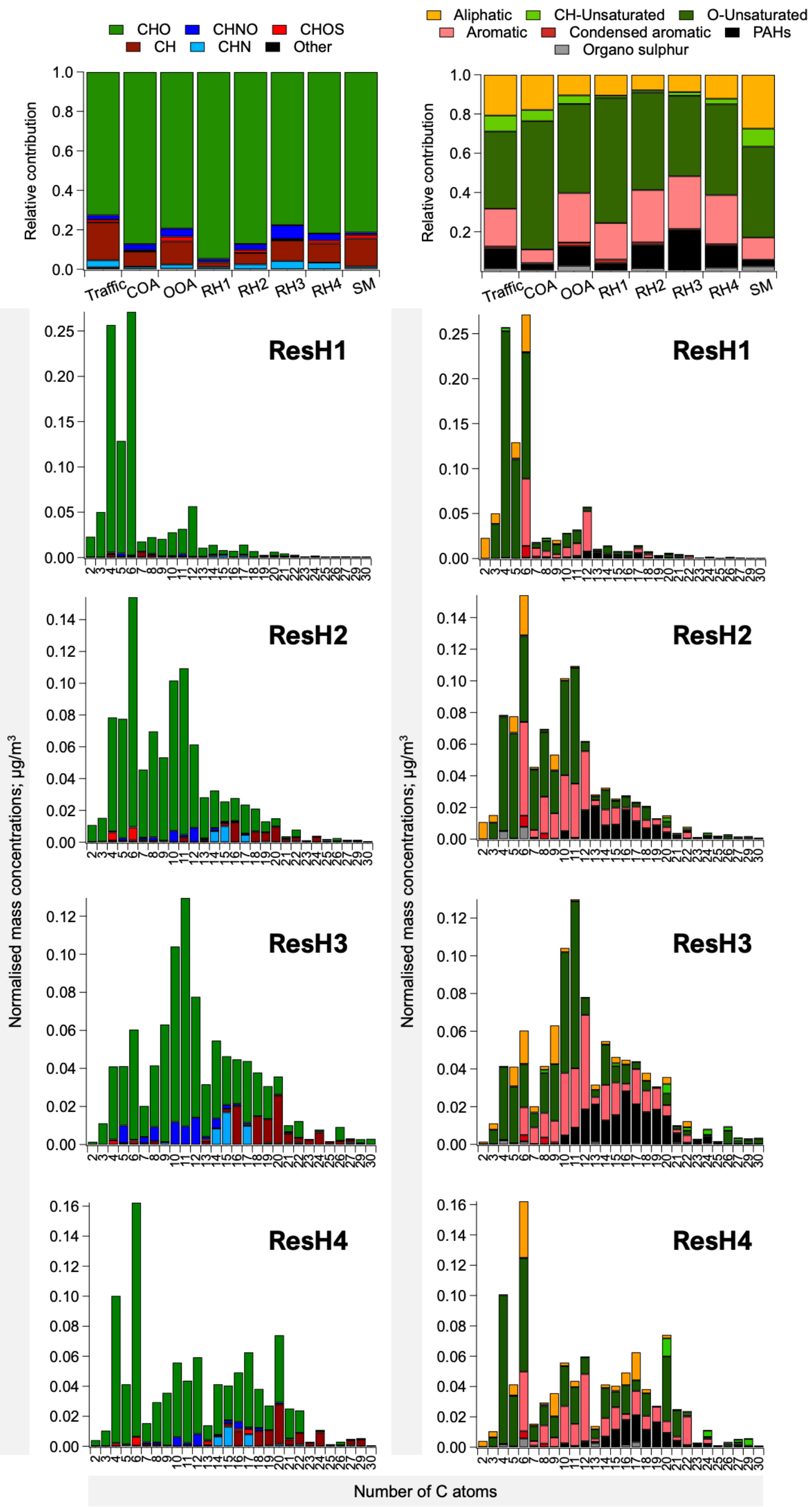

Figure S13. Overview of the distributions of chemical composition and estimated aromaticity of the residential heating factors as a function of the number of C atoms in the species identified and signal contributed by them to each of the factors.

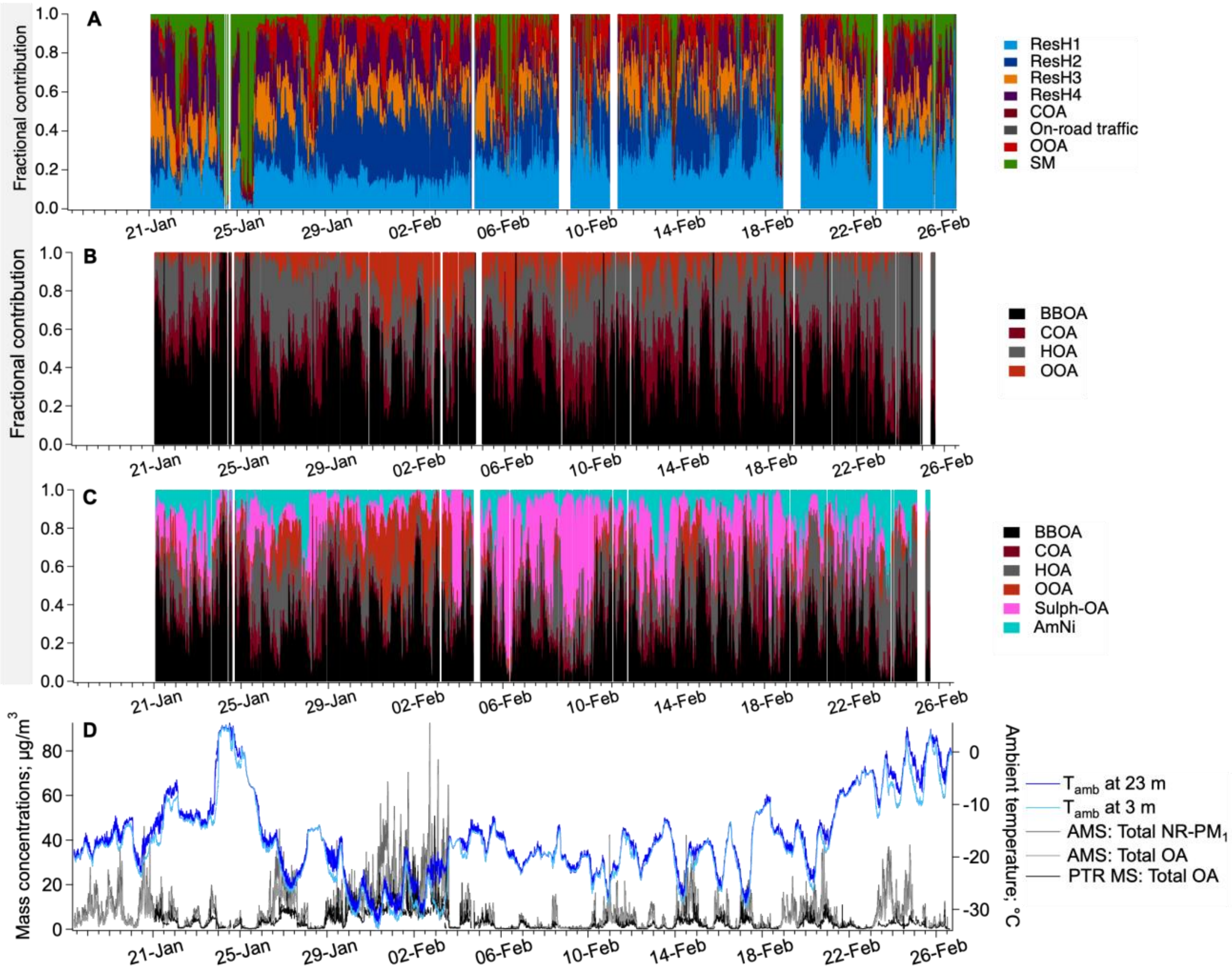

Figure S14. Fractional contributions of the factors identified for the different datasets. (**A**) OA with the $\mathrm{PTR_{CHARON}}$; (**B**) OA with the AMS; and (**C**) $\mathrm{NR\text{-}PM_1}$ with the AMS. Corresponding campaign-averages are given in **Figure 6**; (**D**) Ambient air temperature and absolute mass concentrations of $\mathrm{NR\text{-}PM_1}$ and OA to indicate periods of relatively more importance due to high aerosol loads.

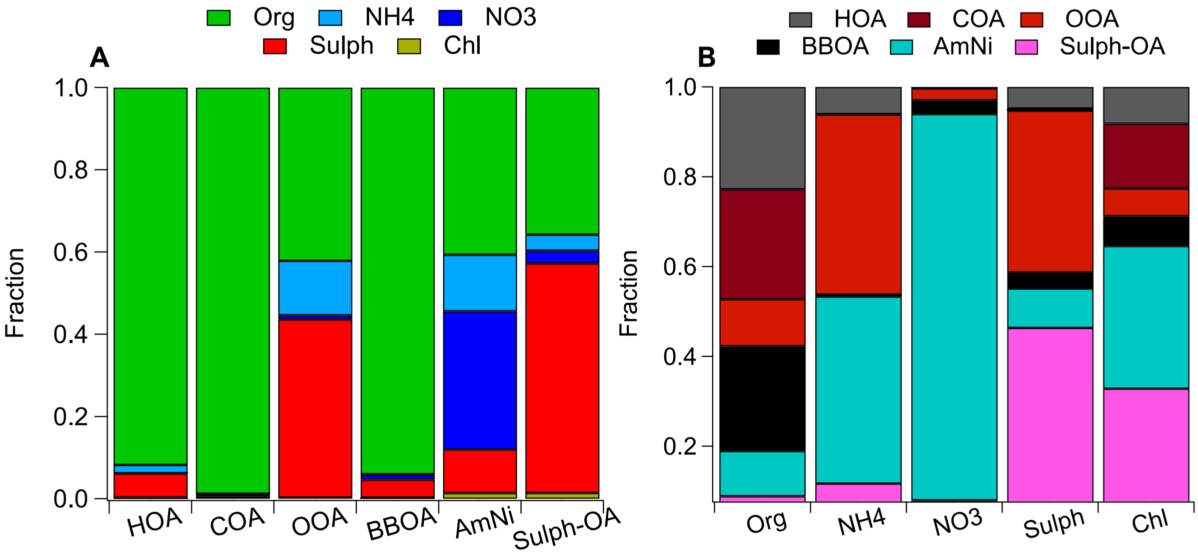

Figure S15. Distribution of organic and inorganic constituents across the six factors identified in $\mathrm{AMS}_{\mathrm{org+inorg}}$ analysis.

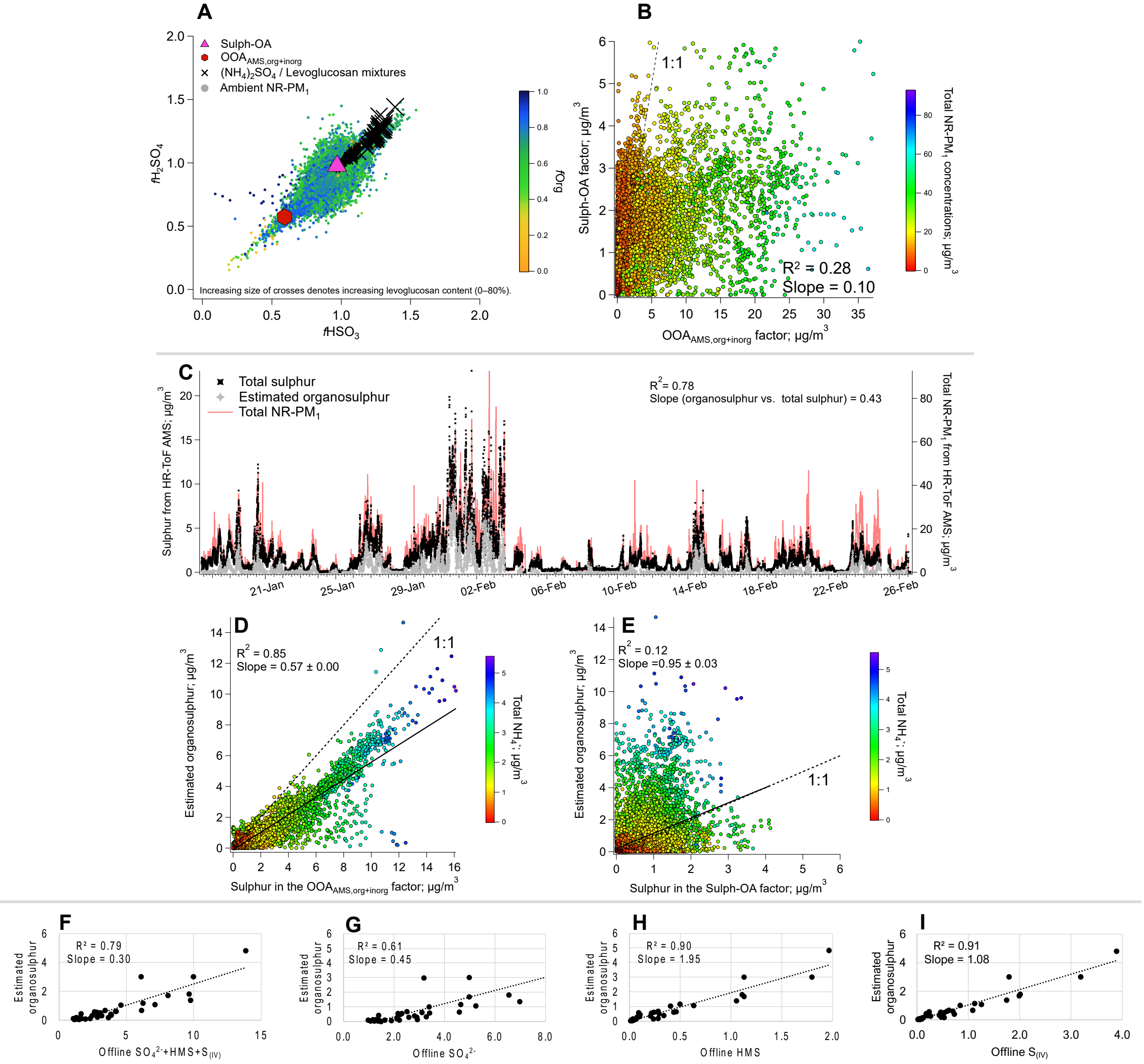

Figure S16. Differentiating between the two sulphur-rich factors in this study, i.e., OOA$_{AMS,org+inorg}$ and sulph-OA. (**A**) Scatter plot of normalised fractions of HSO_3^+ to $H_2SO_4^+$ fragments for the ambient aerosol, OOA$_{AMS,org+inorg}$, sulph-OA, and standard mixtures of pure ammonium sulphate with 0–80% by mass of levoglucosan (inspired by (Chen et al., 2019)); (**B**) scatter plot of the absolute concentrations of OOA$_{AMS,org+inorg}$ and sulph-OA coloured by total NR-PM$_1$ concentrations; (**C**) Times series of estimated concentrations of organosulphur using the method of (Song et al., 2019), along with total sulphur and NR-PM$_1$ from the AMS; (**D–E**) scatter plot showing linear regression ($p < 0.05$) between estimated organosulphur and factors, OOA$_{AMS,org+inorg}$ and sulph-OA. Data points are coloured by total NH_4^+ measured with the AMS; and (**F–I**) Scatter plots showing the correlation (R^2; $p \leq 0.05$) between estimated organosulphur from the AMS and offline ion chromatography of sulphur-containing chemical species in PM$_{0.7}$ collected on filters as part of a separate study (Dingilian et al., 2024).

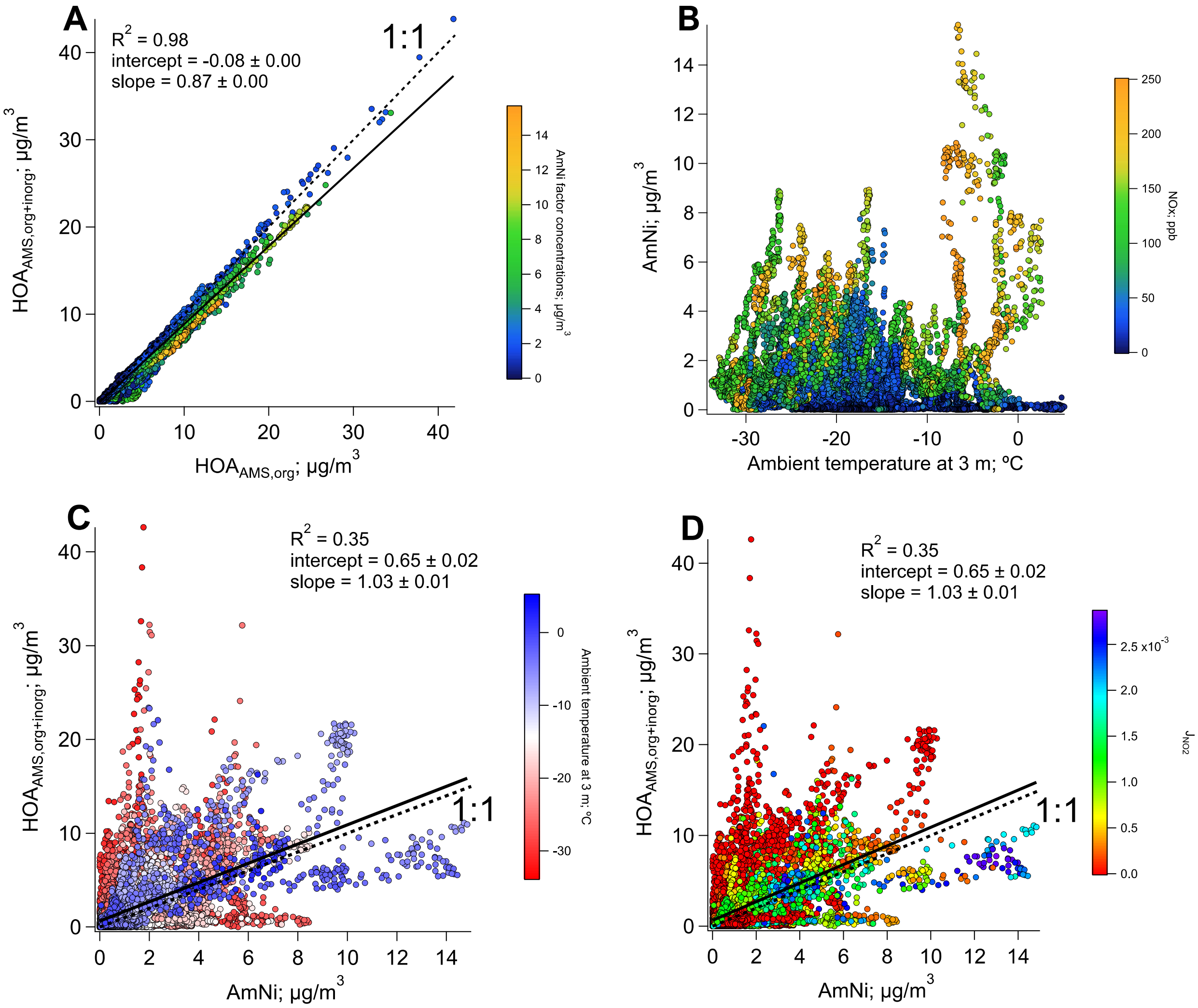

Figure S17. Possible origin and trends of distribution of the AmNi factor during the campaign. (**A**) A scatter plot of the hydrocarbon-like OA (HOA) factor with and without organics shows two "arms" of data points. Data points with higher-than-expected concentrations of the $HOA_{AMS,org}$ coincide with higher AmNi concentrations; (**B**) Distribution of AmNi factor as a function of temperature. Highest concentrations are recorded at > -10ºC and coincide with high NO_x concentrations; (**C–D**) Scatter plot of $HOA_{AMS,org+inorg}$ with AmNi shows comparable concentrations at temperatures above > 10ºC and non-zero J_{NO2} values > 0.5×10^{-3} indicating some sunlight.

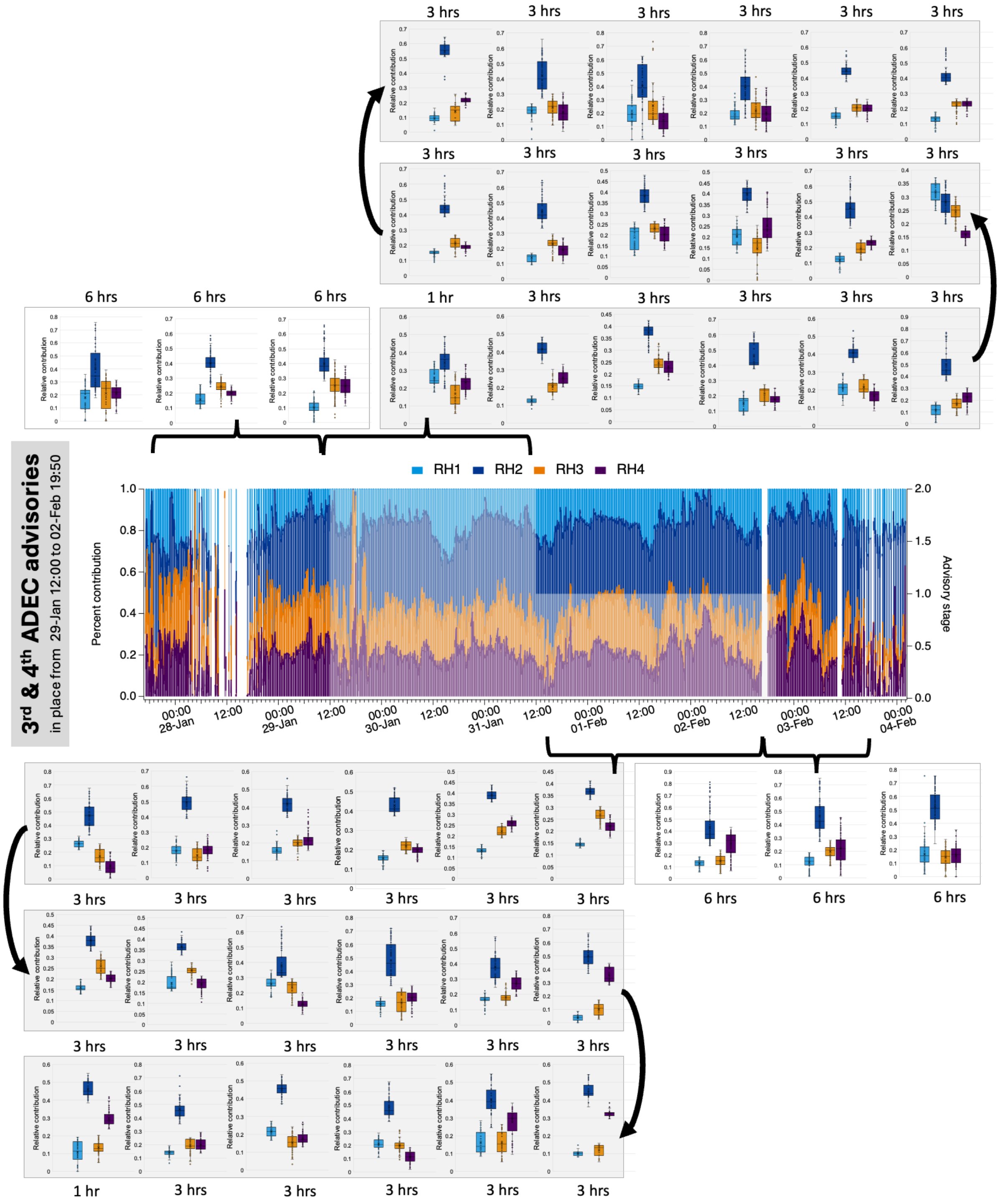

Figure S18. Variation in the relative contributions of residential heating factors to biomass-burning OA concentrations during the 3rd and 4th ADEC advisories. Contributions are also shown for approximately a day before and after the advisory for comparison, along with 6-hour averages as box plots (white panels), when suitable data was available (e.g., periods with noisy data were omitted and the adjacent period is shown instead). For better visualisation of variation in contributions, when the advisory was in place, 3-hour averages are shown (grey panels). To account for a lag in the appearance of variations in emission sources, 1-hour averages are shown for the beginning and end of the advisory event.

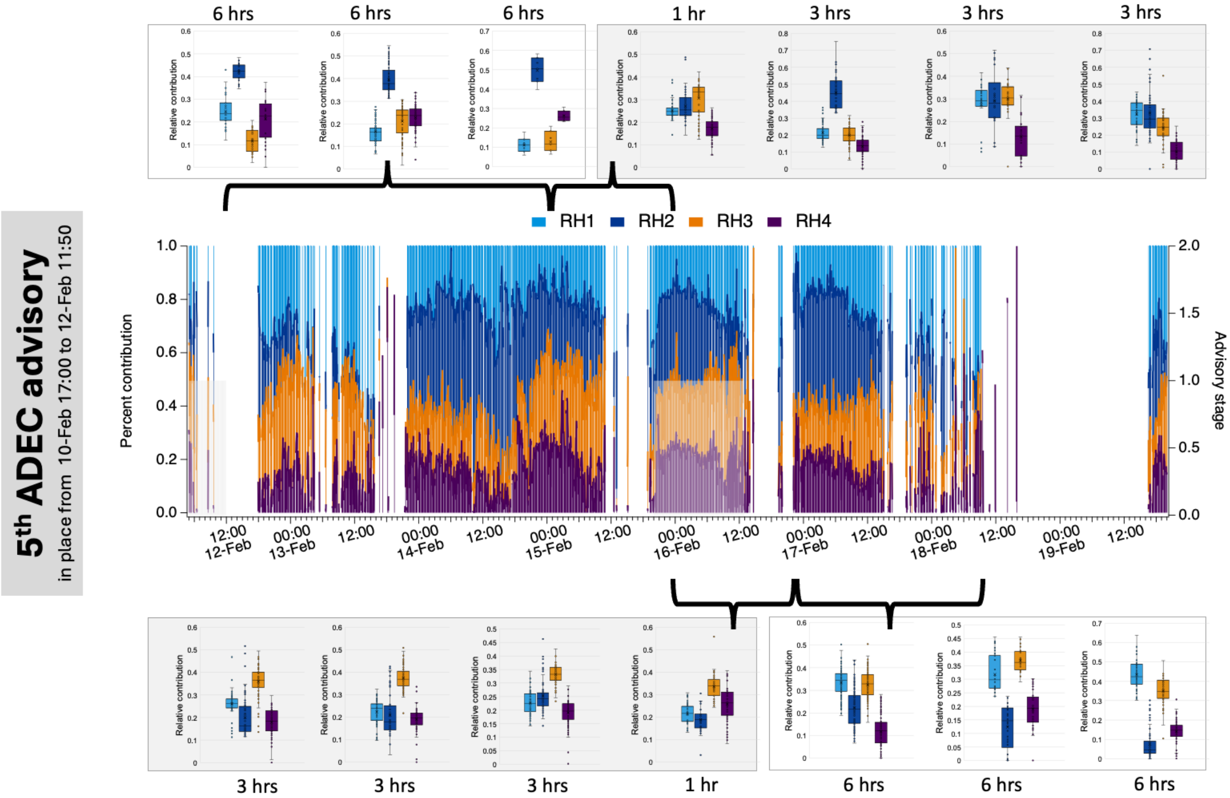

Figure S19. Variation in the relative contributions of residential heating factors to biomass-burning OA concentrations during the 5th ADEC advisory. Contributions are also shown for approximately 2 days before and after the advisory for comparison, along with 6-hour averages as box plots (white panels), when suitable data was available (e.g., periods with noisy data were omitted and the adjacent period is shown instead). For better visualisation of variation in contributions, when the advisory was in place, 3-hour averages are shown (grey panels). To account for a lag in the appearance of variations in emission sources, 1-hour averages are shown for the beginning and end of the advisory event.

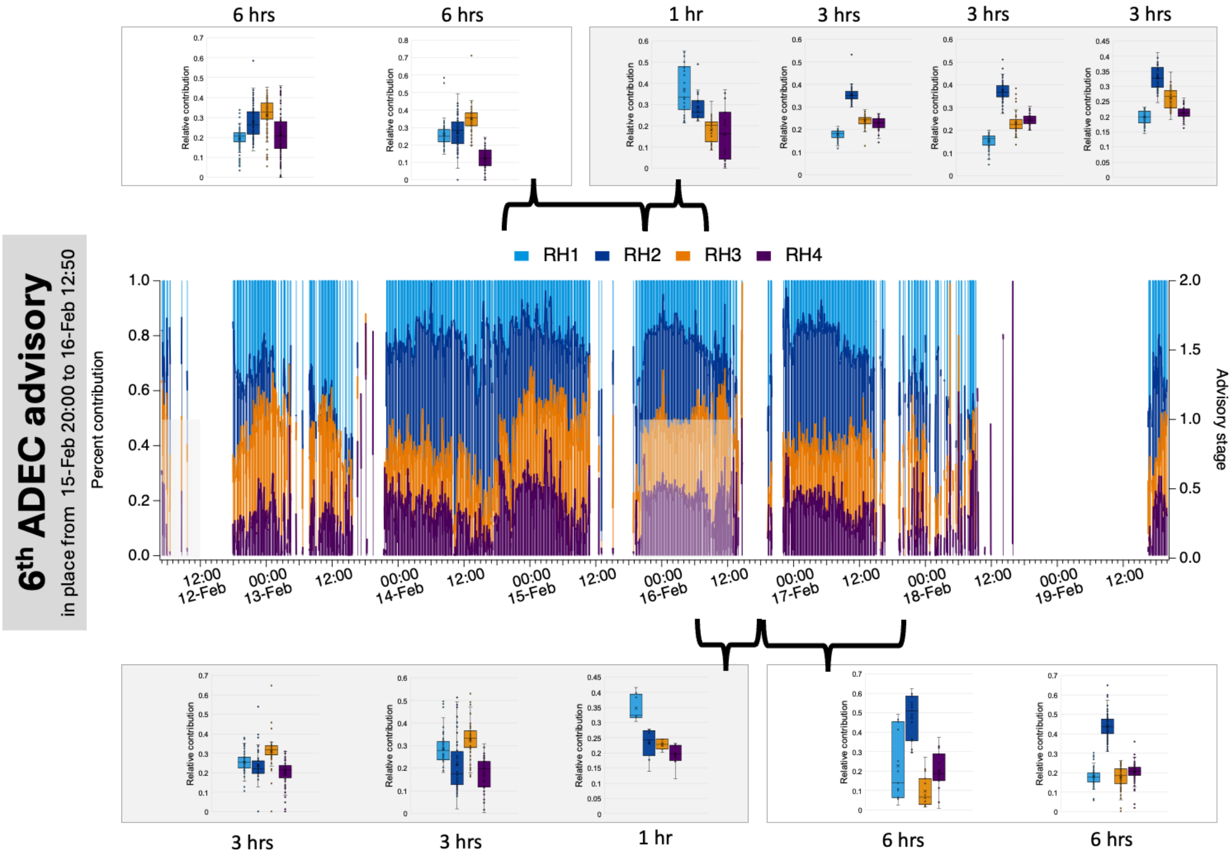

Figure S20. Variation in the relative contributions of residential heating factors to biomass-burning OA concentrations during the 6th ADEC advisory. Contributions are also shown for approximately 2 days before and after the advisory for comparison, along with 6-hour averages as box plots (white panels), when suitable data was available (e.g., periods with noisy data were omitted and the adjacent period is shown instead). For better visualisation of variation in contributions, when the advisory was in place, 3-hour averages are shown (grey panels). To account for a lag in the appearance of variations in emission sources, 1-hour averages are shown for the beginning and end of the advisory event.

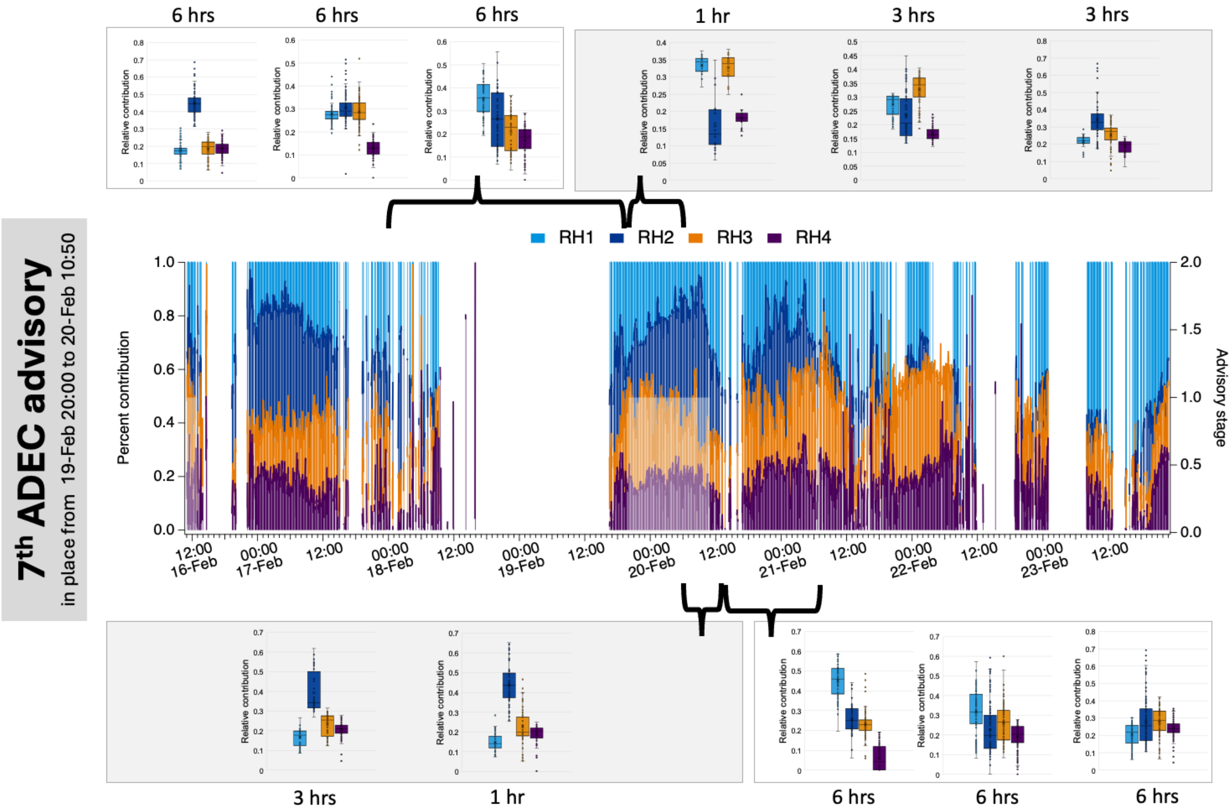

Figure S21. Variation in the relative contributions of residential heating factors to biomass-burning OA concentrations during the 7th ADEC advisory. Contributions are also shown for approximately 2 days before and after the advisory for comparison, along with 6-hour averages as box plots (white panels), when suitable data was available (e.g., periods with noisy data were omitted and the adjacent period is shown instead). For better visualisation of variation in contributions, when the advisory was in place, 3-hour averages are shown (grey panels). To account for a lag in the appearance of variations in emission sources, 1-hour averages are shown for the beginning and end of the advisory event.

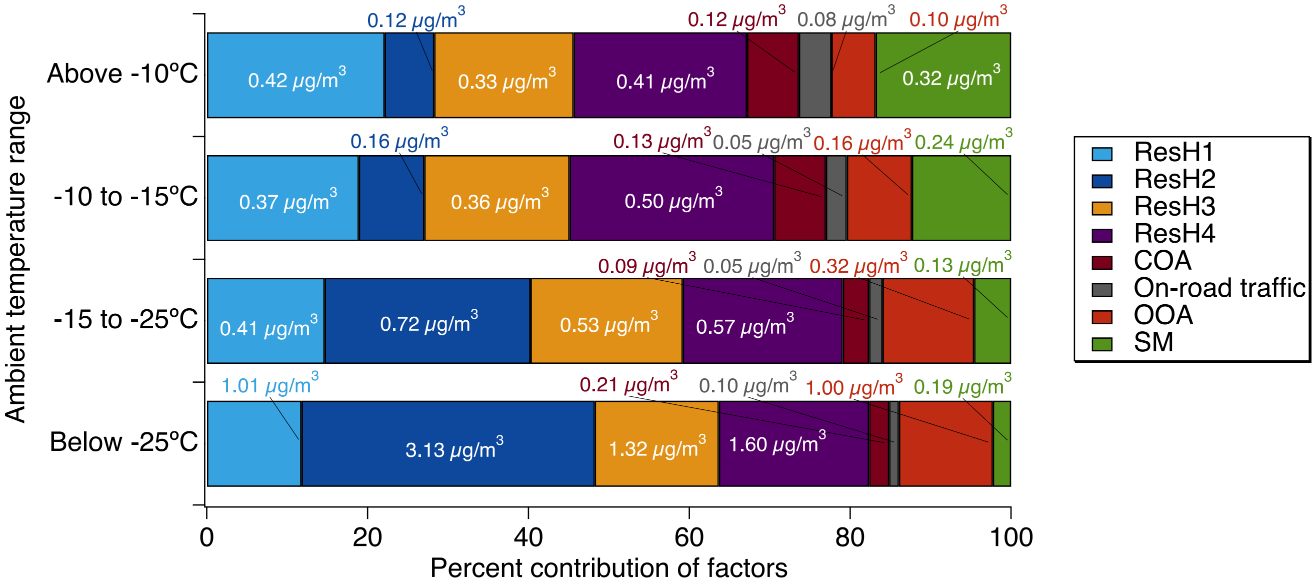

Figure S22. Variation in the absolute mass concentrations and relative contributions of the PTR$_{\text{CHARON}}$ factors with temperature.

Supplementary tables

Table S1 Composition of the calibration gas mixture and the experimental sensitivity obtained in the field.

Compound	***m/z***	***k*-rate (10^{-9} cm^3/sec)**	**Sensitivity$_{start}$ (ncps/ppb)**	**Sensitivity$_{end}$ (ncps/ppb)**
Methanol	33.033	2.36	77	72
Acetonitrile	42.033	4.45	211	194
Acetaldehyde	45.033	3.40	289	207
Acetone	59.049	3.58	317	286
Isoprene	69.069	1.96	151	134
Benzene	79.054	1.93	196	173
Toluene	93.069	2.09	279	247
m-Xylene	107.087	2.27	366	324
1,3,5 Trimethylbenzene	121.101	2.4	462	405
1,2,4,5 Tetramethylbenzene	135.116	2.5	600	521

Table S2 A summary of factors observed in all runs of the constrained analyses to justify the selection of the base-cases (green highlight), other than the environmental explainability of source apportionment (e.g., Q/Q$_{exp}$, residuals, etc.)

Number of factors	**PTR$_{CHARON}$**	**AMS$_{org}$**	**AMS$_{org+inorg}$**
3	No COA or OOA observed, unless constrained	COA not observed, unless it was constrained	COA not observed, unless it was constrained
4	COA observed without constraining; OOA mixed with ResH	**Distinct HOA, COA, OOA, BBOA, even without constraining**	BBOA and OOA factors mixed; COA and HOA mixed
5	Additional distinct ResH; OOA mixed with ResH	HOA split into two very similar factors	COA and HOA mixed
6	OOA was separated but the 3 ResH factors presented some mixing based on inter-factor and with-tracer temporal correlations	HOA split into very similar factors; additional factors with no reasonable physical explanation	**Distinct AmNi, sulph-OA, HOA, COA, OOA, and BBOA factors even without constraining**
7	The SM factor appeared; 3 distinct Res-H factors and one that was mixed with OOA	Factor splitting; additional factor with no reasonable physical explanation	An additional sulphur-rich factor with no reasonable physical explanation
8	**Distinct OOA, COA; 4 distinct ResH factors; no evidence of mixing among the factors**	Factor splitting; additional factor with no physical explanation	Factor splitting; additional factor with no physical explanation
9	An additional factor that was a mix of OOA and ResH	Factor splitting; additional factor with no physical explanation	Factor splitting; additional factor with no physical explanation
10	Evidence of factor splitting along with a factor with OOA and ResH mixed	Factor splitting; additional factor with no physical explanation	Factor splitting; additional factor with no physical explanation

Table S3 Evaluation criteria for the selection of reasonable runs after bootstrapping. SoFi applies each evaluation criterion to extract the factors (in all runs) that satisfy it (Datalystica, 2022). Those factors are then not considered for any other evaluation criteria. Therefore, the sequence in which the different criteria are evaluated in SoFi is crucial to avoid mixing and confusion with the wrong criteria, especially in cases where the same criteria can apply to multiple factors. The position of each criterion in our analyses is given in brackets.

Factor (number of bootstrapped runs, *n*)	**PTR$_{\text{CHARON}}$ (*n* = 125)**	**AMS$_{\text{org}}$ (*n* = 250)**	**AMS$_{\text{org+inorg}}$ (*n* = 250)**
ResH1/BBOA	No evaluation criteria applied	R^2 with *m/z* 60 ≥ 0.70 (**2nd**)	R^2 with *m/z* 60 ≥ 0.70 (**2nd**)
ResH2	R^2 with *m/z* 60.0831 (C_3H_9N; trimethylamine) ≥ 0.70 (**4th**)	--	--
ResH3	R^2 with SO_2 ≥ 0.60 (**6th**)	--	--
ResH4	R^2 with *m/z* 303.2428 ($C_{20}H_{30}O_2$; abietic acid) ≥ 0.80 (**3rd**)	--	--
COA	R^2 with *m/z* 281.2486 ($C_{18}H_{32}O_2$; linoleic acid) ≥ 0.80 (**0th**)	Ratio between the lunch peak (1400 hrs) to morning hours (i.e., average of 0600 and 0700 hrs) (**0th**)	Ratio between the lunch peak (1400 hrs) to morning hours (i.e., average of 0600 and 0700 hrs) (**0th**)
On-road traffic/HOA	R^2 with NO_x ≥ 0.65 (**1st**)	R^2 with NO_x ≥ 0.65 (**1st**)	R^2 with NO_x ≥ 0.65 (**1st**)
OOA	R^2 with *m/z* 97.0653 (C_6H_8O) ≥ 0.80 (**2nd**)	R^2 with NH_4 ≥ 0.75 (**3rd**)	R^2 with NH_4 ≥ 0.85 (**4th**)
SM	R^2 with *m/z* 59.0491 (C_3H_6O; acetone) ≥ 0.60 (**5th**)	--	--
Sulph-OA	--	--	No evaluation criteria applied
AmNi	--	--	R^2 with NO_3 ≥ 0.85 (**3rd**)

Table S4 Linear regression correlations (R^2; $p \leq 0.05$) among the time series of factors derived from different methods. (**A**) PTR_{CHARON} versus AMS_{org}, (B) PTR_{CHARON} versus $AMS_{org+inorg}$, and (C) AMS_{org} versus $AMS_{org+inorg}$. Slopes are given in brackets, for which columns and rows were treated as dependent and independent variables, respectively.

A

	Traffic	COA	OOA	ResH1	ResH2	ResH3	ResH4	SM
HOA	0.48 (0.02)	0.18 (0.02)	0.19 (0.09)	0.22 (0.07)	0.06 (0.15)	0.07 (0.05)	0.04 (0.06)	0.02 (0.01)
COA	0.27 (0.04)	0.47 (0.13)	0.24 (0.36)	0.17 (0.23)	0.06 (0.59)	0.06 (0.18)	0.05 (0.23)	0.03 (0.03)
OOA	0.33 (0.02)	0.17 (0.03)	0.74 (0.24)	0.26 (0.11)	0.23 (0.41)	0.14 (0.11)	0.09 (0.12)	0.09 (0.02)
BBOA	0.12 (0.01)	0.14 (0.03)	0.12 (0.11)	0.51 (0.17)	0.65 (0.76)	0.56 (0.24)	0.66 (0.35)	0.00 (0.00)

B

	Traffic	COA	OOA	ResH1	ResH2	ResH3	ResH4	SM
HOA	0.43 (0.02)	0.15 (0.02)	0.12 (0.08)	0.18 (0.07)	0.05 (0.14)	0.06 (0.05)	0.04 (0.06)	0.01 (0.01)
COA	0.22 (0.04)	0.43 (0.14)	0.23 (0.40)	0.14 (0.24)	0.08 (0.73)	0.05 (0.19)	0.06 (0.27)	0.03 (0.03)
OOA	0.36 (0.01)	0.17 (0.02)	0.68 (0.12)	0.25 (0.06)	0.18 (0.19)	0.13 (0.05)	0.08 (0.05)	0.09 (0.01)
BBOA	0.18 (0.01)	0.15 (0.03)	0.26 (0.14)	0.53 (0.15)	0.72 (0.70)	0.52 (0.20)	0.62 (0.30)	0.02 (0.01)
AmNi	0.26 (0.02)	0.13 (0.03)	0.17 (0.15)	0.11 (0.10)	0.00 (0.05)	0.01 (0.04)	0.00 (0.00)	0.02 (0.01)
Sulph-OA	0.22 (0.04)	0.11 (0.06)	0.31 (0.41)	0.28 (0.30)	0.16 (0.82)	0.33 (0.43)	0.14 (0.38)	0.00 (0.01)

C

	HOA	COA	OOA	BBOA
HOA	0.98 (1.09)	0.18 (0.13)	0.13 (0.30)	0.08 (0.21)
COA	0.17 (1.54)	0.97 (1.11)	0.25 (1.54)	0.15 (1.03)
OOA	0.26 (0.37)	0.20 (0.09)	0.95 (0.51)	0.11 (0.16)
BBOA	0.12 (0.43)	0.18 (0.16)	0.32 (0.53)	0.92 (0.84)
AmNi	0.45 (1.25)	0.24 (0.25)	0.14 (0.49)	0.03 (0.21)
Sulph-OA	0.14 (1.34)	0.11 (0.32)	0.27 (1.28)	0.21 (1.04)

Very strong	≥0.75
Strong	≥0.5 and <0.75
Moderate	≥0.3 and <0.5
Weak	≥0.1 and <0.3
None	<0.1

Table S5 Inter-factor similarity for each instrument. Correlations (R^2; $p \leq 0.05$) among the time series of factors derived from (**A**) PTR$_{\text{CHARON}}$, (B) AMS$_{\text{org}}$, and (C) AMS$_{\text{org+inorg}}$ with all other factors from the same method. Slopes are given in brackets, for which columns and rows were treated as dependent and independent variables, respectively.

A

	Traffic	COA	OOA	RH1	RH2	RH3	RH4	SM
Traffic	1.00							
COA	0.29 (0.24)	1.00						
OOA	0.17 (0.05)	0.11 (0.09)	1.00					
RH1	0.27 (0.08)	0.19 (0.15)	0.18 (0.54)	1.00				
RH2	0.07 (0.01)	0.08 (0.02)	0.15 (0.13)	0.36 (0.16)	1.00			
RH3	0.10 (0.04)	0.12 (0.09)	0.12 (0.34)	0.52 (0.56)	0.41 (1.90)	1.00		
RH4	0.08 (0.02)	0.11 (0.06)	0.06 (0.17)	0.35 (0.32)	0.50 (1.54)	0.55 (0.52)	1.00	
SM	0.06 (0.12)	0.05 (0.28)	0.02 (0.64)	0.00 (0.07)	0.01 (1.54)	0.00 (0.00)	0.01 (0.51)	1.00

B

	HOA	COA	OOA	BBOA
HOA	1.00			
COA	0.21 (1.66)	1.00		
OOA	0.22 (0.64)	0.24 (0.18)	1.00	
BBOA	0.09 (0.43)	0.14 (0.16)	0.13 (0.38)	1.00

Very strong	≥0.75
Strong	≥0.5 and <0.75
Moderate	≥0.3 and <0.5
Weak	≥0.1 and <0.3
None	<0.1

C

	HOA	COA	OOA	BBOA	AmNi	Sulph-OA
HOA	1.00					
COA	0.14 (1.27)	1.00				
OOA	0.16 (0.26)	0.21 (0.08)	1.00			
BBOA	0.09 (0.34)	0.20 (0.15)	0.26 (0.94)	1.00		
AmNi	0.35 (1.00)	0.14 (0.18)	0.15 (0.98)	0.04 (0.29)	1.00	
Sulph-OA	0.11 (1.04)	0.07 (0.23)	0.28 (2.57)	0.24 (1.24)	0.06 (0.48)	1.00

References

Bosque, R. and Sales, J.: Polarizabilities of solvents from the chemical composition, Journal of chemical information and computer sciences, 42, 1154-1163, 2002.

Capozzi, V., Makhoul, S., Aprea, E., Romano, A., Cappellin, L., Sanchez Jimena, A., Spano, G., Gasperi, F., Scampicchio, M., and Biasioli, F.: PTR-MS characterization of VOCs associated with commercial aromatic bakery yeasts of wine and beer origin, Molecules, 21, 483, 2016.

Cappellin, L., Probst, M., Limtrakul, J., Biasioli, F., Schuhfried, E., Soukoulis, C., Märk, T. D., and Gasperi, F.: Proton transfer reaction rate coefficients between H3O+ and some sulphur compounds, International Journal of Mass Spectrometry, 295, 43-48, 2010.

Cappellin, L., Karl, T., Probst, M., Ismailova, O., Winkler, P. M., Soukoulis, C., Aprea, E., Märk, T. D., Gasperi, F., and Biasioli, F.: On quantitative determination of volatile organic compound concentrations using proton transfer reaction time-of-flight mass spectrometry, Environmental science & technology, 46, 2283-2290, 2012.

Chen, Y., Xu, L., Humphry, T., Hettiyadura, A. P., Ovadnevaite, J., Huang, S., Poulain, L., Schroder, J. C., Campuzano-Jost, P., and Jimenez, J. L.: Response of the aerodyne aerosol mass spectrometer to inorganic sulfates and organosulfur compounds: Applications in field and laboratory measurements, Environmental science & technology, 53, 5176-5186, 2019.

Datalystica: Source Finder (SoFi) 8.2 Manual for the software package SoFi (Pro) in IGOR Wavemetrics Inc., 2022.

Dingilian, K., Hebert, E., Battaglia Jr, M., Campbell, J. R., Cesler-Maloney, M., Simpson, W., St. Clair, J. M., Dibb, J., Temime-Roussel, B., and D'anna, B.: Hydroxymethanesulfonate and Sulfur (IV) in Fairbanks Winter During the ALPACA Study, ACS ES&T Air, 2024.

Eichler, P., Müller, M., D'anna, B., and Wisthaler, A.: A novel inlet system for online chemical analysis of semi-volatile submicron particulate matter, Atmospheric Measurement Techniques, 8, 1353-1360, 2015a.

Eichler, P., Müller, M., Klinger, A., Jordan, A., and Wisthaler, A.: CHARON PTR-ToF-MS: a new method for real-time measurement and molecular-level characterization of submicron organic aerosol, 2015b.

Ellis, A. and Mayhew, C.: Chemical Ionization: Chemistry, Thermodynamics and Kinetics, Proton Transfer Reaction Mass Spectrometry, 25-48, 2014.

Gueneron, M., Erickson, M. H., VanderSchelden, G. S., and Jobson, B. T.: PTR-MS fragmentation patterns of gasoline hydrocarbons, International Journal of Mass Spectrometry, 379, 97-109, 2015.

Herring, C. L., Faiola, C. L., Massoli, P., Sueper, D., Erickson, M. H., McDonald, J. D., Simpson, C. D., Yost, M. G., Jobson, B. T., and VanReken, T. M.: New methodology for quantifying polycyclic aromatic hydrocarbons (PAHs) using high-resolution aerosol mass spectrometry, Aerosol Science and Technology, 49, 1131-1148, 2015.

Holzinger, R., Williams, J., Herrmann, F., Lelieveld, J., Donahue, N., and Röckmann, T.: Aerosol analysis using a Thermal-Desorption Proton-Transfer-Reaction Mass Spectrometer (TD-PTR-MS): a new approach to study processing of organic aerosols, Atmospheric chemistry and physics, 10, 2257-2267, 2010.

Juntto, S. and Paatero, P.: Analysis of daily precipitation data by positive matrix factorization, Environmetrics, 5, 127-144, 1994.

Katz, E. F., Guo, H., Campuzano-Jost, P., Day, D. A., Brown, W. L., Boedicker, E., Pothier, M., Lunderberg, D. M., Patel, S., and Patel, K.: Quantification of cooking organic aerosol in the indoor environment using aerodyne aerosol mass spectrometers, Aerosol Science and Technology, 55, 1099-1114, 2021.

Langevin, P.: Sur la loi de recombination des ions, Ann. Chim. Phys, 28, 433-530, 1903.

Leglise, J., Müller, M., Piel, F., Otto, T., and Wisthaler, A.: Bulk Organic Aerosol Analysis by Proton-Transfer-Reaction Mass Spectrometry: An Improved Methodology for the Determination of Total Organic Mass, O: C and H: C Elemental Ratios, and the Average Molecular Formula, Analytical chemistry, 91, 12619-12624, 2019.

Müller, M., Eichler, P., D'Anna, B., Tan, W., and Wisthaler, A.: Direct sampling and analysis of atmospheric particulate organic matter by proton-transfer-reaction mass spectrometry, Analytical chemistry, 89, 10889-10897, 2017.

Pieber, S. M., Kumar, N. K., Klein, F., Comte, P., Bhattu, D., Dommen, J., Bruns, E. A., Kılıç, D., El Haddad, I., and Keller, A.: Gas-phase composition and secondary organic aerosol formation from standard and particle filter-retrofitted gasoline direct injection vehicles investigated in a batch and flow reactor, Atmospheric Chemistry and Physics, 18, 9929-9954, 2018.

Reyes-Villegas, E., Bannan, T., Le Breton, M., Mehra, A., Priestley, M., Percival, C., Coe, H., and Allan, J. D.: Online chemical characterization of food-cooking organic aerosols: Implications for source apportionment, Environmental science & technology, 52, 5308-5318, 2018.

Rivas, I., Beddows, D. C., Amato, F., Green, D. C., Järvi, L., Hueglin, C., Reche, C., Timonen, H., Fuller, G. W., and Niemi, J. V.: Source apportionment of particle number size distribution in urban background and transport stations in four European cities, Environment international, 135, 105345, 2020.

Seinfeld, J. H. and Pandis, S. N.: Atmospheric chemistry and physics: from air pollution to climate change, 3rd, John Wiley & Sons2016.

Sekimoto, K., Li, S.-M., Yuan, B., Koss, A., Coggon, M., Warneke, C., and de Gouw, J.: Calculation of the sensitivity of proton-transfer-reaction mass spectrometry (PTR-MS) for organic trace gases using molecular properties, International Journal of Mass Spectrometry, 421, 71-94, 2017.

Song, S., Gao, M., Xu, W., Sun, Y., Worsnop, D. R., Jayne, J. T., Zhang, Y., Zhu, L., Li, M., Zhou, Z., Cheng, C., Lv, Y., Wang, Y., Peng, W., Xu, X., Lin, N., Wang, Y., Wang, S., Munger, J. W., Jacob, D. J., and McElroy, M. B.: Possible heterogeneous chemistry of hydroxymethanesulfonate (HMS) in northern China winter haze, Atmos. Chem. Phys., 19, 1357-1371, 10.5194/acp-19-1357-2019, 2019.

Stefenelli, G., Pospisilova, V., Lopez-Hilfiker, F. D., Daellenbach, K. R., Hüglin, C., Tong, Y., Baltensperger, U., Prévôt, A. S., and Slowik, J. G.: Organic aerosol source apportionment in Zurich using an extractive electrospray ionization time-of-flight mass spectrometer (EESI-TOF-MS)–Part 1: Biogenic influences and day–night chemistry in summer, Atmospheric Chemistry and Physics, 19, 14825-14848, 2019.

Su, T. and Chesnavich, W. J.: Parametrization of the ion–polar molecule collision rate constant by trajectory calculations, The Journal of Chemical Physics, 76, 5183-5185, 1982.

Temime Roussel, B., Cesler-Maloney, M., Chazeau, B., Ijaz, A., Brett, N., Law, K., Bekki, S., Mao, J., Ketcherside, D., Selimovic, V., Hu, L., Simpson, W. R., and D'Anna, B.: Concentrations and Sources of VOCs during wintertime urban pollution at Fairbanks, Alaska, December 01, 20222022.

Xu, L., Williams, L., Young, D., Allan, J., Coe, H., Massoli, P., Fortner, E., Chhabra, P., Herndon, S., and Brooks, W.: Wintertime aerosol chemical composition, volatility, and spatial variability in the greater London area, Atmospheric Chemistry and Physics, 16, 1139-1160, 2016.

Zhang, Y., Favez, O., Petit, J.-E., Canonaco, F., Truong, F., Bonnaire, N., Crenn, V., Amodeo, T., Prévôt, A. S., and Sciare, J.: Six-year source apportionment of submicron organic aerosols from near-continuous highly time-resolved measurements at SIRTA (Paris area, France), Atmospheric Chemistry and Physics, 19, 14755-14776, 2019.

Zhao, J. and Zhang, R.: Proton transfer reaction rate constants between hydronium ion (H3O+) and volatile organic compounds, Atmospheric Environment, 38, 2177-2185, 2004.

Zografou, O., Gini, M., Manousakas, M. I., Chen, G., Kalogridis, A. C., Diapouli, E., Pappa, A., and Eleftheriadis, K.: Combined organic and inorganic source apportionment on yearlong ToF-ACSM dataset at a suburban station in Athens, Atmospheric Measurement Techniques, 15, 4675-4692, 2022.